nature methods

ARTICLES

https://doi.org/10.1038/s41592-021-01234-z

Automated segmentation and tracking of mitochondria in live-cell time-lapse images

Austin E. Y. T. Lefebvre[1,2], Dennis Ma[3], Kai Kessenbrock[3], Devon A. Lawson[4] and Michelle A. Digman[1,2] ✉

Mitochondria display complex morphology and movements, which complicates their segmentation and tracking in time-lapse images. Here, we introduce Mitometer, an algorithm for fast, unbiased, and automated segmentation and tracking of mitochondria in live-cell two-dimensional and three-dimensional time-lapse images. Mitometer requires only the pixel size and the time between frames to identify mitochondrial motion and morphology, including fusion and fission events. The segmentation algorithm isolates individual mitochondria via a shape- and size-preserving background removal process. The tracking algorithm links mitochondria via differences in morphological features and displacement, followed by a gap-closing scheme. Using Mitometer, we show that mitochondria of triple-negative breast cancer cells are faster, more directional, and more elongated than those in their receptor-positive counterparts. Furthermore, we show that mitochondrial motility and morphology in breast cancer, but not in normal breast epithelia, correlate with metabolic activity. Mitometer is an unbiased and user-friendly tool that will help resolve fundamental questions regarding mitochondrial form and function.

The cell governs our birth, our response to mental and physical wounds, and ultimately our demise. Within these cells, the mitochondrion lies at the intersection of these three physiological states, and understanding its dynamics may help to identify important therapeutic targets for the pharmaceutical treatment of a broad range of diseases, from Alzheimer's disease to cancer[1–3].

The roles that structure and function play in healthy mitochondria and the impact that altered mitochondrial morphology, movement, and fission and fusion dynamics have on the regulation of vital biological processes are currently the subjects of active research. For example, recent studies have demonstrated mitochondria-associated actin accumulation before fission events[4]. Additionally, their localization in neurons has been found to fuel the bioenergy demands at distal extremities[5], regulate the turnover of dysfunctional mitochondria[6], and regulate neurogenesis in postmitotic cells[1]. Impairment of these mitochondrial dynamics has also been associated with a wide variety of neurodegenerative diseases, including Alzheimer's disease[7,8], Huntington's disease[9] and Parkinson's disease[10–12]. It has also been suggested that dysregulation of mitochondrial motion may contribute to the fueling of bioenergy demands in metastatic cancer[13,14]. However, the advancement of both basic and preclinical mitochondria research has been held back by the biased and time-consuming manual analysis methods currently serving as the gold standard in the field. To uncover the peculiarities of these important life-preserving and disease-driving organelles, a novel method for automated and robust mitochondrial segmentation and tracking must first be developed.

Existing segmentation and tracking methods are difficult to tailor to mitochondria because of their dynamics and unique shapes. Several general techniques exist, but they make use of a Gaussian fit to estimate morphology, which works well only for spherical and elliptical particles[15–17]. Object-based tracking methods are better suited for mitochondrial morphologies because they allow for variability in size and shape. Importantly, these methods require unbiased segmentation of the objects to be tracked, which is non-trivial. A deep learning model has been constructed for mitochondrial segmentation and it includes transfer learning, to train the model in one's own system, although manual annotation is required, which may introduce bias[18]. Other deep learning models tailored broadly to biological segmentation may also be adapted to organellar segmentation, but they are still in their early stages and are not yet consistently used[19,20]. Current methods for tracking mitochondria are also limited, most of which work only for linear axonal transport in neurons, and require extensive user input[21–24]. These methods also ignore fission and fusion events altogether, or else require high temporal resolution to connect overlapping regions between frames[25,26]. We compare several of these open-source techniques (Supplementary Note 1, Supplementary Table 1 and Supplementary Figs. 1, 2)[17,18,25,27–30].

To address the issues in analyzing mitochondrial dynamics, we developed Mitometer, a software package that incorporates a new method in a fast, unbiased and automated approach to segmentation and spatiotemporal tracking of mitochondria in live-cell fluorescence microscopy time-lapse images. Mitometer requires only pixel size and the time between frames to identify changes in mitochondrial morphology, motion, and fission and fusion dynamics. We validate our segmentation and tracking algorithms in silico via mitochondria simulations, and in vitro on a panel of cell types with differing basal mitochondrial morphologies, and with influencers of mitochondrial motion, fission and fusion. Using Mitometer we analyze heterogeneities between non-cancerous normal breast epithelial mitochondria, receptor-positive breast cancer (estrogen receptor or progesterone receptor positive; ER/PR+) mitochondria, and triple-negative breast cancer (TNBC) mitochondria from patient-derived xenograft (PDX) breast cancer cells, primary breast cells, and various breast cancer cell lines in both two-dimensional (2D) and three-dimensional (3D) environments. These results show TNBC mitochondria to be faster, more directional and more

[1]Department of Biomedical Engineering, University of California, Irvine, Irvine, CA, USA. [2]Laboratory for Fluorescence Dynamics, Irvine, CA, USA. [3]Department of Biological Chemistry, University of California, Irvine, Irvine, CA, USA. [4]Department of Physiology and Biophysics, University of California, Irvine, Irvine, CA, USA. ✉e-mail: mdigman@uci.edu

elongated than their ER/PR+ counterparts. We further examined correlations between metabolic heterogeneity and the mitochondrial morphology and motility of mitochondria at the level of the single mitochondrion. We found a positive relationship between fractions of bound nicotinamide adenine dinucleotide in its reduced form (NADH) and features such as speed and displacement, and negative relationships with features such as directionality and branching in both TNBC and ER/PR+ mitochondria, but not in normal breast epithelial mitochondria. Together, the automated segmentation and tracking algorithms and the intuitive user interface make Mitometer a broadly accessible tool that requires only basic fluorescence imaging capabilities, and which will serve to advance mitochondrial research in basic science and its clinical applications.

Results

Object-based segmentation of mitochondria. Mitometer takes a 3D or 2D time series of mitochondrial fluorescence images (Fig. 1a). First, we apply a diffuse background removal algorithm to each time frame and *z*-plane of the series (Extended Data Fig. 1 and Supplementary Note 2). This diffuse background subtraction algorithm allows for a size- and shape-independent method of keeping well-isolated mitochondria intact, such as perilamellar mitochondria, and of separating mitochondria in crowded environments, such as perinuclear mitochondria (Fig. 1b, Extended Data Fig. 1 and Supplementary Video 1).

Next, we convolve a Gaussian kernel with the diffuse background-subtracted image to remove high-frequency noise, which is followed by an intensity threshold to create a mask of the segmented mitochondria (Supplementary Note 3). To ensure the stability of the mask, we run a parameter exploration algorithm to select the standard deviation of the kernel and the threshold level (Fig. 1c). A mismatch between these parameters results in improper connections or separations of mitochondria (Extended Data Fig. 2). The optimal parameters minimize the variation in the number and area of mitochondria between adjacent temporal frames of the image while maximizing the median number of mitochondria detected (Fig. 1d, Extended Data Fig. 2 and Supplementary Video 1). We then remove any detected objects below and above predefined minimum and maximum area thresholds and multiply the mask by the original image (Fig. 1e and Supplementary Video 1). In 3D images, we conduct the parameter exploration on the frame with the largest mean intensity value and use the parameters for all layers in the stack. Mitometer performs semantic segmentation by assigning all true pixels in the final binary mask to a mitochondrion. This is followed by a connected-component instance segmentation in which all spatially connected true pixels in the final mask belong to an individual mitochondrion, whereas pixels separated by false pixels belong to different mitochondria. The mitochondria now having been properly segmented, tracking can be accurately performed.

Object-based tracking of mitochondria. Mitochondria are dynamic organelles that undergo translational motion via molecular motors, fission by proteins such as dynamin-related protein 1 (Drp1), fusion by proteins such as mitofusin 1/2 (Mfn1/2) and optic atrophy 1 (Opa1), organic appearance via mitochondrial biogenesis or movement into the plane of focus, and organic disappearance via mitophagy or movement out of the plane of focus[31–33]. For translational motion, a mitochondrion is assigned to its track from the previous frame. In the case of fission, one mitochondrion splits into two or more. In the case of fusion, two or more mitochondria merge into one mitochondrion. Fission and fusion events are differentiated from a mitochondrion's organic appearance and disappearance via a volume (or in two dimensions, area) comparison of new and lost tracks to existing tracks.

Our tracking algorithm uses a frame-by-frame global optimization scheme for track assignment, while allowing new tracks to be made and old tracks to be left unassigned. We first assign each mitochondrion in the first temporal frame to a new track. In each subsequent temporal frame, we assign each mitochondrion to either an existing track or to a new track. Global assignments are determined by a cost minimization scheme of the weighted and *z*-score-normalized differences in six (or, in three dimensions, seven) morphological parameters, that is, the area (or volume), the major and minor (and *z*) lengths, the solidity, the perimeter (or surface area), and the mean intensity of each mitochondrion, along with the difference in intensity-weighted centroid positions between frames (Fig. 2a, Extended Data Fig. 3 and Supplementary Note 4). If a mitochondrion has a high correspondence in all parameters to a mitochondrion of an existing track, the cost of assignment between them will be low, while two mitochondria that have a low correspondence will have a high cost of assignment (Fig. 2b). We also give a cost to assigning a mitochondrion to a new track. Additionally, to ensure the avoidance of highly improbable assignments and to increase the efficiency of our algorithm, we ignore the costs of assigning mitochondria to tracks that violate two defined thresholds: the maximum velocity threshold and the maximum search time threshold (Extended Data Fig. 3). The maximum velocity threshold is the furthest distance a mitochondrion can be from a potential track between frames, derived both empirically and from existing literature[34], and the maximum search time threshold is the maximum number of temporal frames between which a mitochondrion can be assigned to an unassigned track (Supplementary Note 5 and Supplementary Fig. 3).

Each mitochondrion has a track that minimizes the assignment cost for that individual mitochondrion, which may be a different track than one that globally minimizes the assignment of all mitochondria in that frame (Extended Data Fig. 3). We define the assignments that both individually and globally minimize the cost as confident assignments. We calculate the 98th quantile of the running list of confident assignment costs and designate this adaptive cost as the cost of assigning a mitochondrion to a new track (which we initially set to 1 for the first temporal frame, equivalent to 1 standard deviation above the mean cost of all assignments) (Extended Data Fig. 3). We further define a track consisting entirely of confident assignments at the end of the track assignment process as a confident track. For every confident track, we calculate the coefficient of variation (CoV) of each morphological parameter in the track (intraCoV), and between different tracks (interCoV). We use the numeric interCoV : intraCoV ratio normalized to the number of weighted variables (seven in three dimensions, six in two dimensions) as the weighting for each morphological parameter in our cost matrix; conceptually, parameters differing greatly between different tracks will be given a higher weighting, while parameters differing greatly in the same track will be given a lower weighting (Fig. 2c and Supplementary Note 6). We then rerun the tracking algorithm using these calculated weights to improve assignments (Extended Data Fig. 3).

To account for mistakenly disconnected tracks, we apply a stack-wide gap-closing scheme between new and lost tracks (Fig. 2d and Supplementary Note 7). We merge every combination of new and lost tracks that satisfies the velocity and search time thresholds. We then retain as candidates those combinations with a travel angle CoV below 20% (Extended Data Fig. 4). Next, we globally minimize the cost of closure based on the intensity-weighted centroid displacement between viable new and lost track candidates. We also merge any new tracks that have only one possible assignment to a lost track based on velocity and search time thresholds. We iterate through this scheme until the number of tracks ceases to change (Extended Data Fig. 4).

Finally, we discriminate between fission events and organic appearance in new tracks, and fusion events and organic disappearance in lost tracks to detect and quantify these mitochondrial

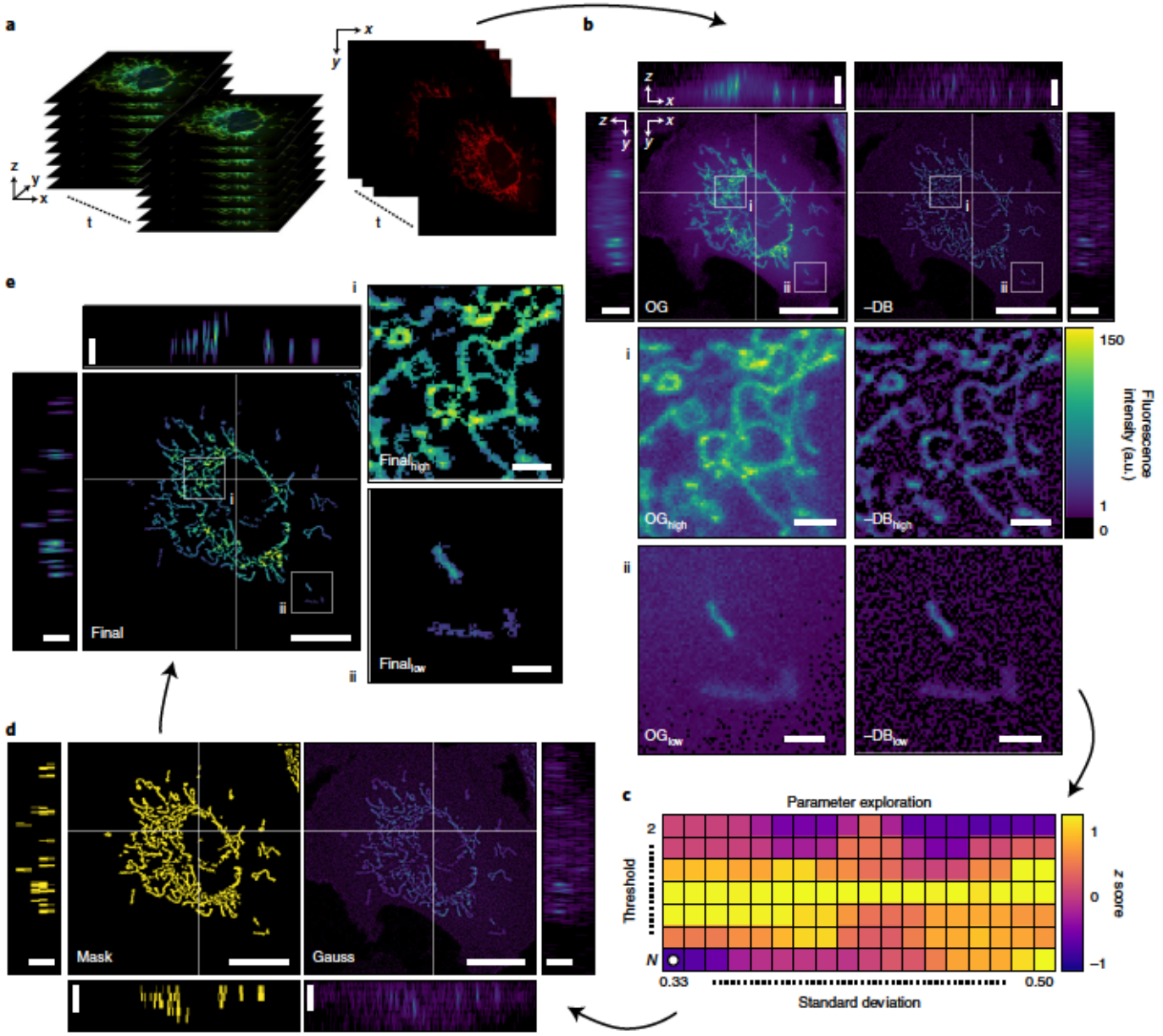

Fig. 1 | Object-based segmentation of individual mitochondria from fluorescence images. a, A 3D or 2D time stack of mitochondrial fluorescence images is taken as an input. **b**, The original (OG) stack (left), with orthogonal *z* projections of white crosshairs is shown. This stack is run through a diffuse background (DB) subtraction algorithm to remove noise between adjacent mitochondria. An example of a perinuclear region with a high DB (i) and a perilamellar region with a low DB (ii) are shown. **c**, A parameter exploration scheme iterates through combinations of Gaussian filter standard deviations and absolute thresholds, and the resulting time stack's connected components are analyzed for variability in number and size throughout the stack. This produces a specific minimum value (white dot) at the optimal parameters. **d**, The optimal Gaussian filter (right) and the intensity and area thresholds are applied to the stack to produce a binary mask (left). **e**, The binary mask is multiplied with the original stack to produce the final stack used for tracking. Scale bars, 20 μm for full images, 2 μm for close-ups. This example is a depiction of a BT-549 cell with mitochondrially targeted mCherry via a lentiviral expression system.

dynamics. We build a list of fission and fusion candidates within the search time threshold of those tracks with extrema distances within the velocity threshold of the new or lost track. We use the extrema distance rather than intensity-weighted centroid distance given that fission or fusion events would result in the appearance or disappearance of two adjacent extrema, respectively. In the case of fission, we limit the possible candidates from which a mitochondrion has split by performing a volume (or area, in two dimensions) threshold by calculating the absolute difference of the mean volume of the track before fission and the sum of the mean volumes of the two tracks after fission (Fig. 2e). In the case of fusion, we instead calculate the absolute difference of the mean volume of the track after fusion and the sum of the mean volumes of the two tracks before fusion (Fig. 2f). To retain the track as a possible fission and fusion candidate, it must meet stringent requirements to ensure a high accuracy while keeping false-positive assignments low (Supplementary Note 8).

In silico validation of segmentation and tracking algorithms. To validate Mitometer, we simulate mitochondrial objects in silico and assign dynamic events to them. This allows us to generate ground truth tracks of mitochondria with varying magnitudes of directed motion, with the ability to appear and disappear, and to undergo

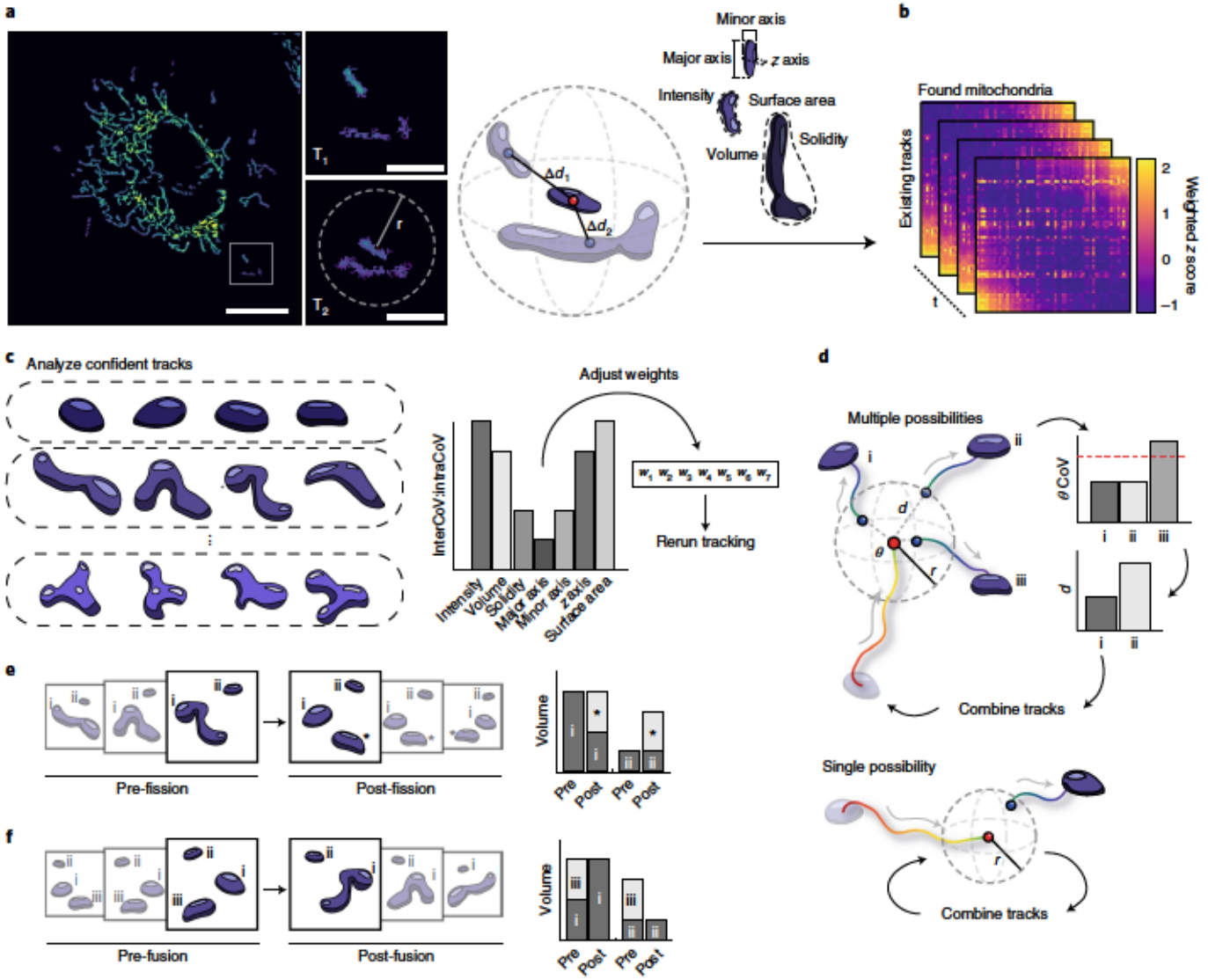

Fig. 2 | Tracking of mitochondria via global minimization of morphological and displacement differences. a,**b**, Mitochondria in the first (T_1) and second (T_2) temporal frames. Scale bars: left, 20 μm; right, 4 μm. Center-of-mass distances (Δd_1, Δd_2) and differences in morphological features within the maximum velocity threshold (r) are used to create a z-score-normalized assignment cost matrix. **c**, Confident mitochondrial tracks and their interCoV : intraCoV ratio for each morphological parameter used for weighting. **d**, In the case of multiple possibilities, gap-closing within r is done via travel angle (θ) and center-of-mass distance (d) of the tracks at the new and lost positions. In the case of a single possible combination, the tracks are combined. **e**, Fission between existing tracks (i,ii) and a newly created track (*) is determined by comparisons of the volume (or area, in two dimensions) and of the extrema distances of nearby mitochondria before and after fission. **f**, Fusion is handled the same way as fission, but compares the volume (or area) and the extrema distances of nearby mitochondria before (i–iii) and after fusion (i,ii).

fusion and fission events (Supplementary Note 9). We did not use manually annotated datasets because these are subjective and are known to generate large position estimation errors in general tracking tasks, as compared with computational tracking methods[35–37].

We test Mitometer's segmentation robustness with regard to the separation of adjacent mitochondria by simulating two parallel mitochondria with an applied Gaussian blur. We vary both the distance of their nearest pre-blur extrema and the signal-to-noise ratio (SNR), as defined by the mean intensity of the generated mitochondria divided by the standard deviation of the background. We separate out the algorithm's detection into four categories: 0, 1, 2, and >2 mitochondria found. In 3 independent trials, the segmentation algorithm faithfully recovers both mitochondria, even with low SNRs and separation distances, and performs better than existing segmentation routines (Fig. 3a and Supplementary Fig. 1).

We test Mitometer's segmentation robustness with regard to the detection of mitochondria of varying sizes by simulating a 5×5 grid of mitochondria while varying both the length of the major axis and the SNR. We separate out the algorithm's detection into three categories: <25, 25, and >25 mitochondria found. Mitometer's segmentation algorithm recovers all 25 mitochondria in most cases of reasonable SNR, again outperforming competing routines (Fig. 3b and Supplementary Fig. 1).

Given that many mitochondrial dyes are sensitive to membrane potential, which may vary widely between mitochondria in a single cell, we also test Mitometer's segmentation robustness with regard to detecting mitochondria of varying intensities. We simulate a 5×5 grid of mitochondria in which each mitochondrion has a different intensity. We vary the range of intensities and the length of the major axis. Mitometer's segmentation algorithm recovers all 25

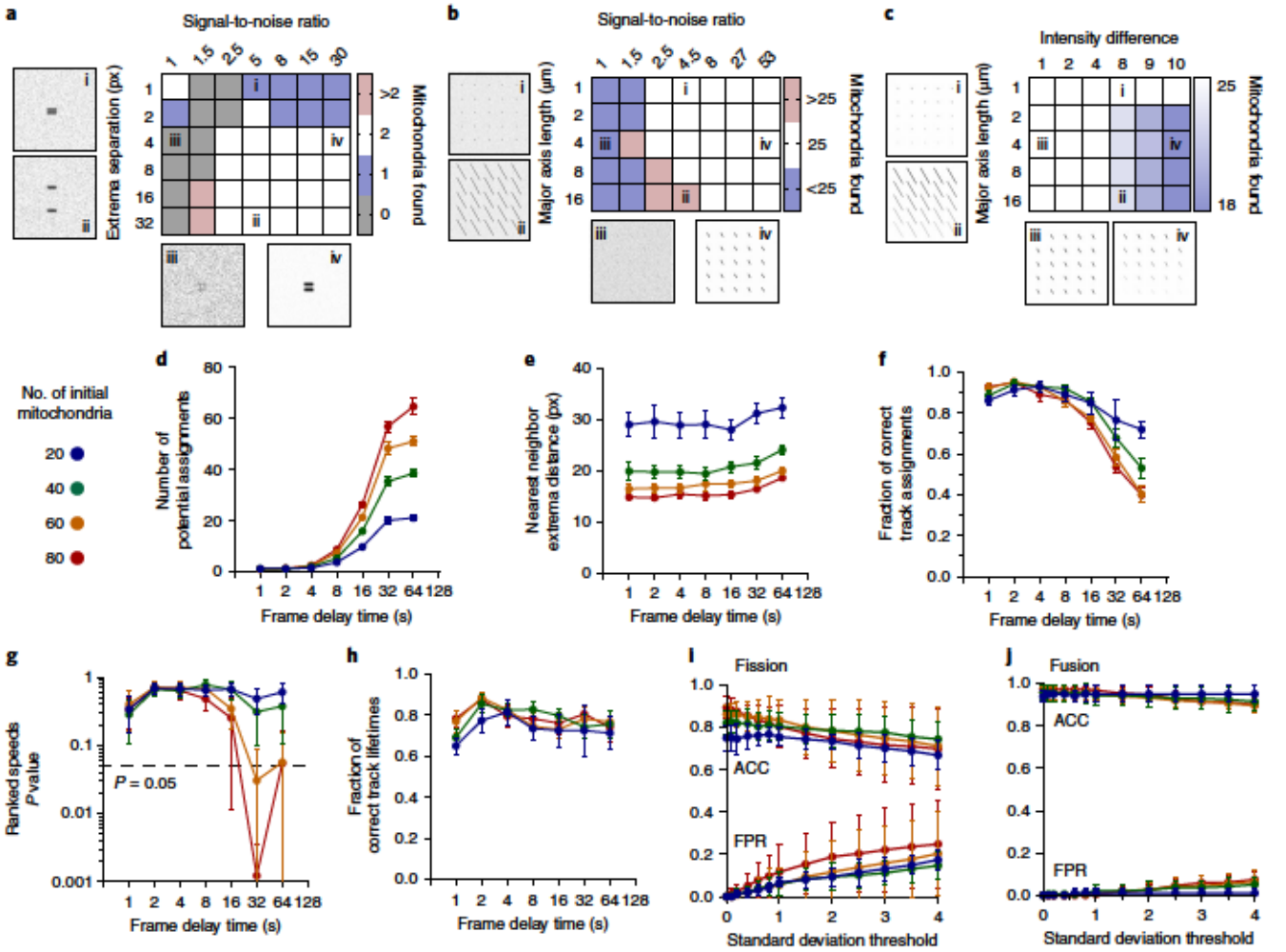

Fig. 3 | In silico validation of mitochondria segmentation and tracking algorithms. a, Two adjacent mitochondria are simulated at increasing separations and signal-to-noise ratios. The median number of mitochondria recovered by the segmentation algorithm is shown. **b**,**c**, A grid of 25 mitochondria is simulated at increasing major axis lengths and signal-to-noise ratios (**b**) or intensity differences (**c**). **d**–**j**, The mean number of mitochondria recovered by our segmentation algorithm is shown. Twenty (blue), 40 (green), 60 (orange) or 80 (red) mitochondria are simulated in the center quarter of a 512× 512 image in two dimensions with a pixel size of 0.138 μm. The mean number of potential assignments of individual mitochondria (**d**) and mean distance to their nearest neighbor (**e**) are shown. The performance of the tracking algorithm compared with ground truth values is quantified by its ability to correctly assign tracks (**f**), the rank sum *P* value of the mitochondrion speeds between the algorithm and the ground truth (two-sided Wilcoxon rank sum test) (**g**), and the fraction of tracks with correct lifetimes (**h**). The mitochondria are then allowed to undergo fission and random appearance (**I**) or fusion and random disappearance (**J**), and the algorithm is quantified in its classification ability according to accuracy (ACC) and false-positive rate (FPR). **d**–**J**, Data are given as the mean and 95% confidence interval. **a**–**c**, $n=3$ independent trials; **d**–**h**, $n=10$ independent trials; **I**,**J**, $n=5$ independent trials.

mitochondria in most cases and detects at least 18 mitochondria in the most difficult tests, again outperforming almost all competing routines (Fig. 3c and Supplementary Fig. 1).

We validate Mitometer's tracking robustness by simulating mitochondria under four conditions of increasing densities. We also vary the delay time between each frame, to produce larger and smaller mitochondrial displacements between frames. In all cases, the number of potential track assignments for each mitochondrion is greater than 1 and increases as the frame delay time increases, as expected (Fig. 3d). We confirm that the average nearest neighbor distance decreases as we increase the density of mitochondria, and increases only slightly for increasing frame delay times as the mitochondria move out from the center of the field where they are generated (Fig. 3e). We quantify Mitometer's performance based on three important metrics, as compared with ground truth values: the fraction of correct assignments between mitochondria in adjacent frames, the rank sum *P* value of the mitochondrion speeds between our algorithm and the ground truth, and the fraction of correct lifetimes of the mitochondrial tracks (Fig. 3f–h). Mitometer performs well in all three metrics at reasonable frame delay times, and outcompetes existing techniques, but drops steadily at high frame delays (Supplementary Fig. 2). The increase in nearest neighbor distance probably accounts for the increase in the ranked speeds *P* value at the longest delay time, which is also seen in other tracking software.

We further validate Mitometer's ability to correctly identify fission and fusion events. As described previously, Mitometer's algorithm compares the track areas before and after fission or fusion and adds a track as a candidate if the area difference is below 1 standard deviation. We tested the algorithm's ability to detect fission and fusion in these simulated conditions with different standard deviation classifications. Mitometer's algorithm had a high classification accuracy and rarely labeled false-positive events at standard deviations below 1 (Fig. 3i,j). As expected, the algorithm performed worse as we increased the standard

deviation threshold, and allowed more events to be classified as fission or fusion.

In vitro validation of segmentation and tracking algorithms. Although in silico experiments are useful when ground truth data are not available, the full characteristics of a complex system in living cells cannot yet be fully represented in a simulation. Thus, we also validate Mitometer in live mammalian cells.

To validate segmentation robustness in vitro, we compare morphologies of mitochondria in three cell types with differing basal mitochondrial morphologies labeled with tetramethylrhodamine methyl ester perchlorate (TMRM): neoblastic pheochromocytoma 12 cells with circular mitochondria, non-small cell lung carcinoma H1299 cells with intermediately elongated mitochondria, and human foreskin fibroblast (HFF) cells with highly elongated mitochondria (Fig. 4a). We compare elongation by quantifying differences in the ratio of the minor axis to the major axis lengths of individual mitochondria. A higher ratio indicates more circular mitochondria, with 1 being a perfect circle. The segmentation algorithm was able to capture the differences in elongation between these three cell types across all tested microscope systems, including an LSM 710 and 880 (Zeiss), Eclipse Ti-E (Nikon), FluoView 1000 (Olympus) and IX83 (Olympus) in total internal reflection fluorescence (TIRF) mode and widefield mode (Fig. 4b). We further validate the segmentation efficiency at differing full well depth and read noise root mean square values by adding artificial Poissonian and Gaussian noise to the time lapses in the same three cell lines. We compared area values to the original time lapse and found that the algorithm performs with high precision at typical detector parameters, and only begins to fail for extremely poor-quality detectors (Extended Data Fig. 5a).

To validate the tracking robustness in cultured cells, we use nocodazole to inhibit mitochondrial motion in the same three cell lines[38]. Nocodazole is a well-studied drug that destabilizes microtubules and inhibits their polymerization, thereby disrupting the physical structures used for mitochondrial movement[39]. As expected, mitochondrial speed in all cell lines dramatically decreased with nocodazole treatment (Fig. 4c and Supplementary Video 2). We validate the tracking efficiency by adding artificial Poissonian and Gaussian noise. We compared mitochondrial speed with the original time lapse and found that the algorithm again only begins to fail at values of extremely poor-quality detectors (Extended Data Fig. 5b).

Finally, to validate the fission and fusion detection robustness in vitro, we use known inducers of fission and fusion and quantify the dynamic events of the cells before and after treatment in a time-dependent manner. For these experiments, we use 10 µM oligomycin to induce fission, and nutrient starvation using Hank's balanced salt solution (HBSS) to induce fusion[40,41]. We chose to use TMRM-labeled Henrietta Lacks (HeLa) cervical cancer cells and mouse embryonic fibroblast (MEF) cells because both cell lines have been previously validated to respond to nutrient starvation in an expected manner (Fig. 4d)[40,42]. To account for variability in the number of mitochondria in various cells, we normalize each time point's fission and fusion events to the average number of events in the three time points acquired before treatment. We then compare these events by normalizing to the controls' events at each time point. We successfully validate in both MEF and HeLa cells an increase in fission and fusion events after treatment with oligomycin or HBSS (Fig. 4e,f).

Together, these experiments confirm Mitometer's robustness and verify the ability of Mitometer's algorithm to properly segment, track and identify fission and fusion events in mitochondria.

Mitochondrial features may predict breast cancer subtype. Mitometer enables us to quantify and compare mitochondrial morphology, motility and dynamics in both 2D and 3D images of mitochondria. We demonstrated these capabilities through a comprehensive analysis of TMRM-labeled mitochondria in a wide panel of breast cells, including five primary normal breast epithelial cell lines from reduction mammoplasties of five different individuals (patients 72, 76, 08, 99, 97), two ER/PR+ breast cancer cell lines (MCF-7, T-47D), three TNBC cell lines (MDA-MB-231, MDA-MB-468, BT-549) and two TNBC PDX cell lines[43] (HCI-010, HCI-002), all of which are detailed in the supplementary materials (Supplementary Table 2). We cultured all these cell lines in a Matrigel-embedded 3D spheroid environment, as previously established[44], as well as an additional 2D culture environment for the two ER/PR+ lines (MCF-7, T-47D) and three TNBC lines (MDA-MB-231, MDA-MB-468, BT-549) (Fig. 5a,b, Extended Data Fig. 6 and Supplementary Videos 3,4).

We compared mitochondria of breast cancer categories (normal epithelia, ER/PR+ and TNBC) in their respective 3D and 2D environments, and also compared mitochondria between 3D and 2D environments in their respective breast cancer categories, using Mitometer. We construct tracks of 3D and 2D mitochondrial displacement while retaining morphological information of every mitochondrion in each frame (Fig. 5c). Simple comparisons of the mean-squared displacement of individual mitochondria show large heterogeneity across cell types (Fig. 5d). We analyzed three motility parameters in each individual mitochondrion across all cell lines and environments: their median speed, their directionality (calculated as the maximum displacement divided by the total distance traveled), and the ratio of the median to the maximum speed (suggesting the propensity for mitochondria to have bursts of motion) (Supplementary Fig. 5). To remain cell size agnostic when constructing the models, instead of using total displacement or distance traveled, we use our directionality metric by dividing the maximum displacement of a track by its total distance traveled (a value necessarily constrained between 0 and 1). In 3D cultures, mitochondria are slower and more directional, with a lower propensity for bursts of motion than their 2D groups (Fig. 5e–g). Interestingly, this phenomenon is consistent at the cellular level during cell migration, in which 3D cultures move slowly but more directionally than their 2D counterparts[45]. Additionally, at the 3D level, mitochondria in breast cancer cells are significantly slower than those of normal breast epithelia, hinting at mitochondrial dysregulation within the cancerous conditions. We also compared the fission and fusion occurrences in 2D cell cultures and noted a lowered odds ratio of fusion, but not fission, in TNBC cells compared with ER/PR+ cells (Fig. 5h). Interestingly, the suppression of mitochondrial fusion in TNBC cells has been shown to enhance breast cancer cell migration and invasion[46]. The results hint at an involvement of mitochondrial dynamics in the increased aggressiveness seen in cases of TNBC compared with cases of ER/PR+ breast cancer. We further analyzed five morphological parameters: the length of mitochondrial minor axes, the length of the major axes, their ratio (which gives the sphericity of the mitochondria), the solidity (calculated as the ratio of the volume of individual mitochondria to their convex hull, which gives information on how branched the mitochondria are), and the mean TMRM fluorescence intensity in individual mitochondria (which gives information on the membrane potential) (Supplementary Fig. 5)[47]. In general, ER/PR+ cells have mitochondria that are less networked and which have higher membrane potentials compared with TNBC mitochondria, but are more rounded only in 2D cultures (Fig. 5i–m). However, there seems to be large heterogeneity in mitochondrial membrane potential and solidity between cell lines, even in the same cancer subtypes, necessitating more in-depth analysis, which is beyond the scope of this paper (Supplementary Fig. 6). Interestingly, TNBC mitochondria are more similar in all parameters to normal breast epithelial mitochondria than to ER/PR+ mitochondria in 3D cultures. Together, these results reinforce a role for mitochondria in breast cancer aggressiveness through the

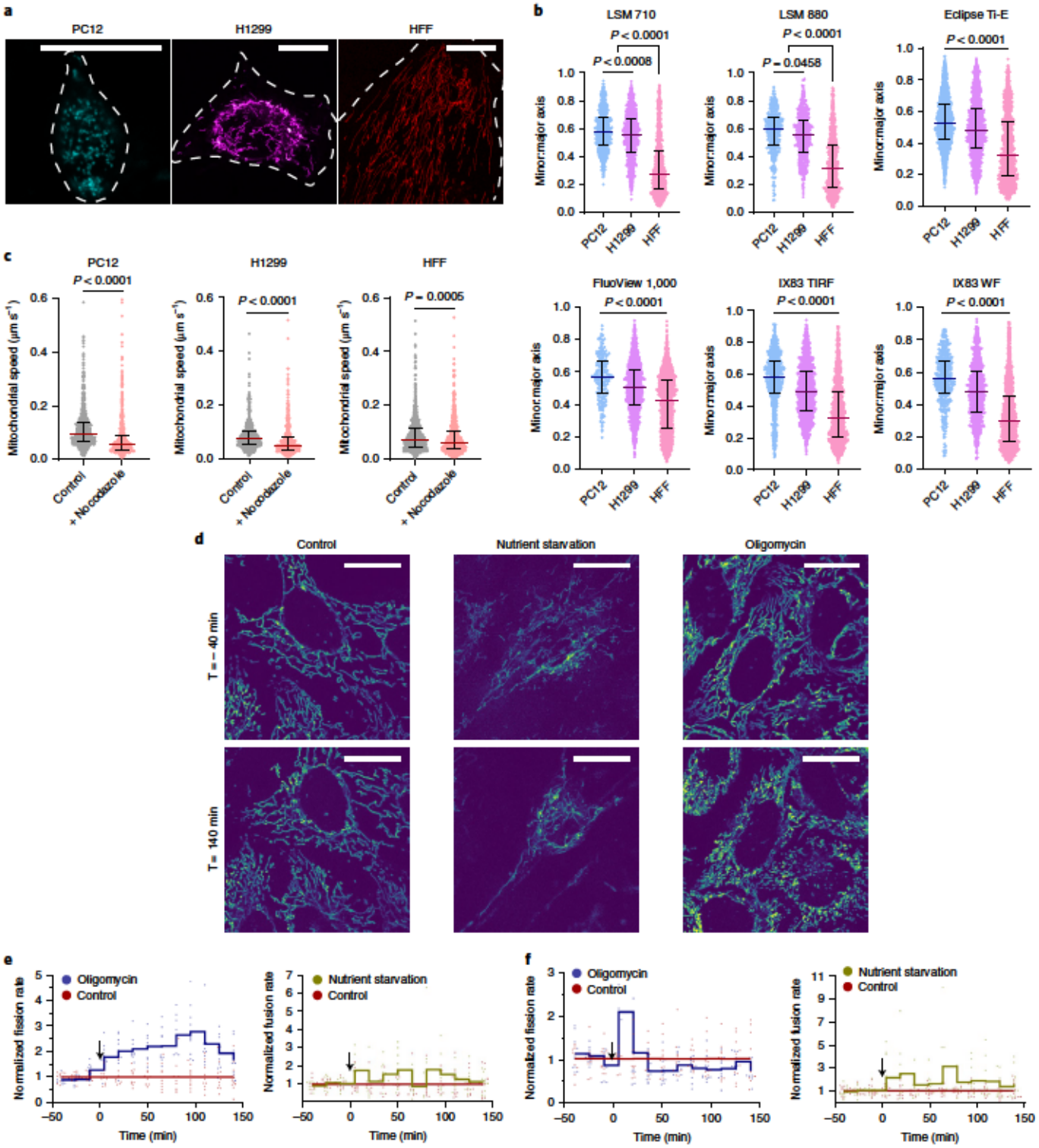

Fig. 4 | In vitro validation of mitochondria segmentation and tracking algorithms. a, Representative images of pheochromocytoma (PC)12, H1299 and HFF cells labeled with TMRM, and their outlines (white dotted lines). **b**, The minor : major axis ratios of each cell line for microscopes LSM 710 (n = 683, 1,047 and 1,218 distinct mitochondrial tracks for PC12, H1299 and HFF cells, respectively), LSM 880 (n = 384, 542, 1,048), Eclipse Ti-E (n = 2,057, 1,369, 1,195), FluoView 1000 (n = 201, 1,640, 1,690), and IX83 in total internal reflection fluorescence (TIRF) mode (n = 793, 1,377, 1,239) and widefield (WF) mode (n = 416, 1,244, 1,658). **c**, The median mitochondrial speeds of PC12 cells (n = 709 and 667 distinct mitochondrial tracks for control and nocodazole-treated conditions, respectively), H1299 cells (n = 563, 475) and HFF cells (n = 835, 604) before and after treatment with 10 μM nocodazole. **d**, Representative images of HeLa (control, oligomycin) or MEF (nutrient starvation) cells 40 min before (top row) or 140 min after (bottom row) no treatment (control), nutrient starvation, and treatment with 10 μM oligomycin. **e**,**f**, Normalized fission (left) and fusion (right) rates of MEF (**e**) and HeLa (**f**) cells before and after (black arrow) no treatment (control; red line), nutrient starvation (yellow line) and 10 μM oligomycin (blue line). n = 10 cells. Data are given as the median and interquartile range (**b**,**c**) or the mean (**e**,**f**). P values are calculated using a Kruskal–Wallis non-parametric rank test with Dunn's post-hoc test (H = 873.5, 540.1, 518.8, 281.5, 621.3, 664.8) (**b**) or using a two-tailed Kolmogorov–Smirnov test (D = 0.3912, 0.2883, 0.1088) (**c**). Scale bars, 20 μm.

modulation of specific morphological and motile mechanisms, and reaffirm the importance of culture environment for the study of cellular processes.

We are also able to predict with high accuracy whether a mitochondrion belongs to an ER/PR+ cancer cell or to a TNBC cell in both 2D and 3D environments. We used a random forest classification through Python's Scikit-learn with a 70:30 train:test split on 8,065 ER/PR+ and 15,022 TNBC mitochondria in the 2D environment, and 670 ER/PR+ and 1,320 TNBC mitochondria in the 3D environment. For classification, we used either morphological characteristics, motility characteristics, or both combined (Supplementary Tables 3,4 and Supplementary Fig. 7)[48]. We achieve an area under the curve (AUC) of the receiver operating characteristic (ROC) curves of above 0.5 in all cases, with the best AUCs of 0.77 and 0.80 for 2D environments and 3D environments, respectively, resulting from the combination of morphological and motility characteristics as an input for predicting mitochondria from ER/PR+ and TNBC subtypes (Fig. 5n,o). The random forest classifier also assesses the feature importance, with median speed ranking highest in the case of the 2D environment, and intensity ranking highest in the case of the 3D environment (Fig. 5p).

Metabolism of single mitochondria via Mitometer and NADH FLIM. We also used Mitometer to analyze the metabolism of single dynamic mitochondria in live normal breast epithelial, ER/PR+ and TNBC cells. We make use of a well-established technique, the phasor approach to the fluorescence lifetime imaging (FLIM) of intrinsically fluorescent and endogenously expressed NADH, to quantify metabolic alterations[49–51]. We labeled the mitochondria of the cells with 100 nM TMRM, a concentration lower than those that affect mitochondrial respiration[52]. We collected NADH and TMRM fluorescence in two separate detectors while simultaneously acquiring FLIM data from the NADH emission in the frequency domain (Supplementary Note 15). We use the rule of linear addition of two components to calculate the fraction of bound NADH (NADHb) of each mitochondrion that is tracked for at least 20 frames (Fig. 6a). A much more detailed explanation of the use of the rule of linear addition for calculating NADH fractions can be found in our previous work[51]. We find that mitochondrial NADHb in each breast cell subtype follows a normal distribution, but that normal breast epithelial cells have a significantly lowered mean NADHb than that of breast cancer cells (Fig. 6b,c). We also find that these normal cells have more variation in their NADHb compared with cancerous breast cells, as calculated using the CoVs (Fig. 6d). We further analyze how mitochondrial motility and morphology parameters correlate with respect to mitochondrial NADHb (Fig. 6e). Again, to ensure that we remain cell size agnostic when deriving correlations between mitochondrial parameters and bound NADH values, we analyze mitochondria only within the same cell, rather than correlating these values in bulk across all samples. This also allows us to account for natural variations in both TMRM labeling efficiency and basal NADH fractions between different cells. We find few significant correlations in any parameters in normal breast epithelial cells, except for a small positive correlation in perimeter and a negative correlation in solidity. By contrast, mitochondria in both ER/PR+ and TNBC cancer cells had highly significant correlations in a wide array of parameters. Most notably, mitochondria in breast cancer cells had positive correlations of NADHb with mitochondrial speed and displacement, and negative correlations of NADHb with solidity, directionality and TMRM intensity. Interestingly, mitochondria in ER/PR+ cancer cells had higher correlation coefficients than those in TNBC cells in every tested parameter. These results suggest an association between changes in mitochondrial metabolism and changes in mitochondrial motility and morphology in breast cancer cells, but not in normal breast epithelial cells, and may identify therapeutic vulnerabilities to specifically target breast cancer cells. To determine if these feature differences are brought about due to changes in metabolism, we treated MDA-MB-231 cells with 5 µM antimycin A, an inhibitor of mitochondrial electron transport chain complex III. Treatment induced a lowering of cell-wide NADHb as expected (Fig. 6f). We then performed an analysis of the three most positively and negatively NADHb-correlated mitochondrial parameters. Surprisingly, antimycin A treatment led to an increase in mitochondrial median, mean and maximum speeds, and decreases in solidity, directionality,and mean fluorescence intensity, all of which are the inverse of the calculated correlations with NADHb (Fig. 6g–l). This suggests that mitochondrial motility and morphological features do not directly depend on NADHb and that instead, specific mitochondria in individual cells are modulated to perhaps serve specific metabolic needs. This also represents an analysis of metabolic alterations in relation to mitochondrial motility and morphology at the level of the single mitochondrion in living cells.

Discussion

Mitometer is an efficient resource for quickly and accurately analyzing morphological and motility features of mitochondria that eliminates the need for time-consuming and biased user intervention. We optimize and automate segmentation techniques to maintain the integrity of mitochondrial morphology for object-based tracking. The minimization scheme used for tracking allows for computational efficiency and an accurate and automated track construction process. Furthermore, the use of an object-based tracking method allows for determination of fission and fusion events via comparison of mitochondrial volumes. Simulations and experiments with cell lines of heterogeneous mitochondria, nocodazole,

Fig. 5 | Motility and morphology differences in mitochondria of normal breast epithelial cells and breast cancer cells. a, Tracks of mitochondria overlaid on fluorescence images of a TNBC MDA-MB-231 cell line (left) and an ER/PR+ MCF-7 cell line (right) stained with TMRM and imaged for 2 min at 1 s intervals. **b**, Tracks and corresponding *z*-stack time-lapse images of TMRM fluorescence in non-cancerous (control) primary breast epithelial cell spheroids (left), ER/PR+ MCF-7 spheroids (middle) and TNBC MDA-MB-231 spheroids (right) **c**, A single mitochondrial track (left) of an MDA-MB-231 (top) and MCF-7 (bottom) cell with the detected mitochondrial object's morphology shown overlaid (right), downscaled 10-fold relative to the track length. **d**, A mean-squared displacement (MSD) graph of the tracks (i) and (ii) shown in **a** and **b**. **e–g**, The speed (**e**), directionality (**f**), and median:maximum speed ratio (**g**) of normal primary epithelial cells (control 1–5), ER/PR+ cells (MCF-7, T-47D) and TNBC PDX cells and cell lines (HCI-010, HCI-002, MDA-MB-231, MDA-MB-468, BT-549) in 3D and 2D environments. **h**, The fission and fusion odds ratio of TNBC cell lines compared with ER/PR+ cell lines in a 2D environment. **i–m**, The major (**i**) and minor (**j**) axes lengths, axes ratio (**k**), solidity (**l**) and mean TMRM fluorescence intensity (**m**) of normal, ER/PR+ and TNBC cells in 3D and 2D environments. $n = 868$, 670, 1,320, 8,065 and 15,022 distinct mitochondrial tracks in 3D normal, ER/PR+ and TNBC cells, and 2D ER/PR+ and TNBC cells, respectively. **n,o**, ROC curves of random forest classifications between mitochondria from ER/PR+ cells and TNBC cells using only morphological characteristics (blue), motility characteristics (purple) or both (yellow) in 2D (**n**) and 3D (**o**) environments, with the AUC. **p**, Importance of features used for the random forest classification in 2D and 3D environments. Data are given as the mean ± s.d. (**d**,**h**) or median and interquartile range (**e–g**,**i–m**). *P* values are calculated using a two-sided Fisher's exact test (**h**) or a Kruskal–Wallis non-parametric rank test with a post-hoc Dunn's multiple comparison test ($H = 4542$, 390.0, 335.0, 103.1, 53.12, 734.8, 516.5, 873.5) (**e–g**,**i–m**, respectively). Scale bars, 20 µm (**a**), 10 µm (**b**) and 1 µm (**c**).

and fission- and fusion-inducing agents validated the robustness of the algorithms. Validation experiments confirmed the robustness of the algorithms, with cases of failure occurring only at low SNRs (~1.5) and low mitochondrial separation (~2 pixels), and for simulated parameters of especially poor (~800 full well depth) detectors.

We have demonstrated Mitometer's ability to detect small but important differences in morphology and motility in the mitochondria of TNBC, ER/PR+, and normal breast cells in clinically relevant PDX TNBC models, primary mammary cells, and well-established breast cancer cell lines. These results will have

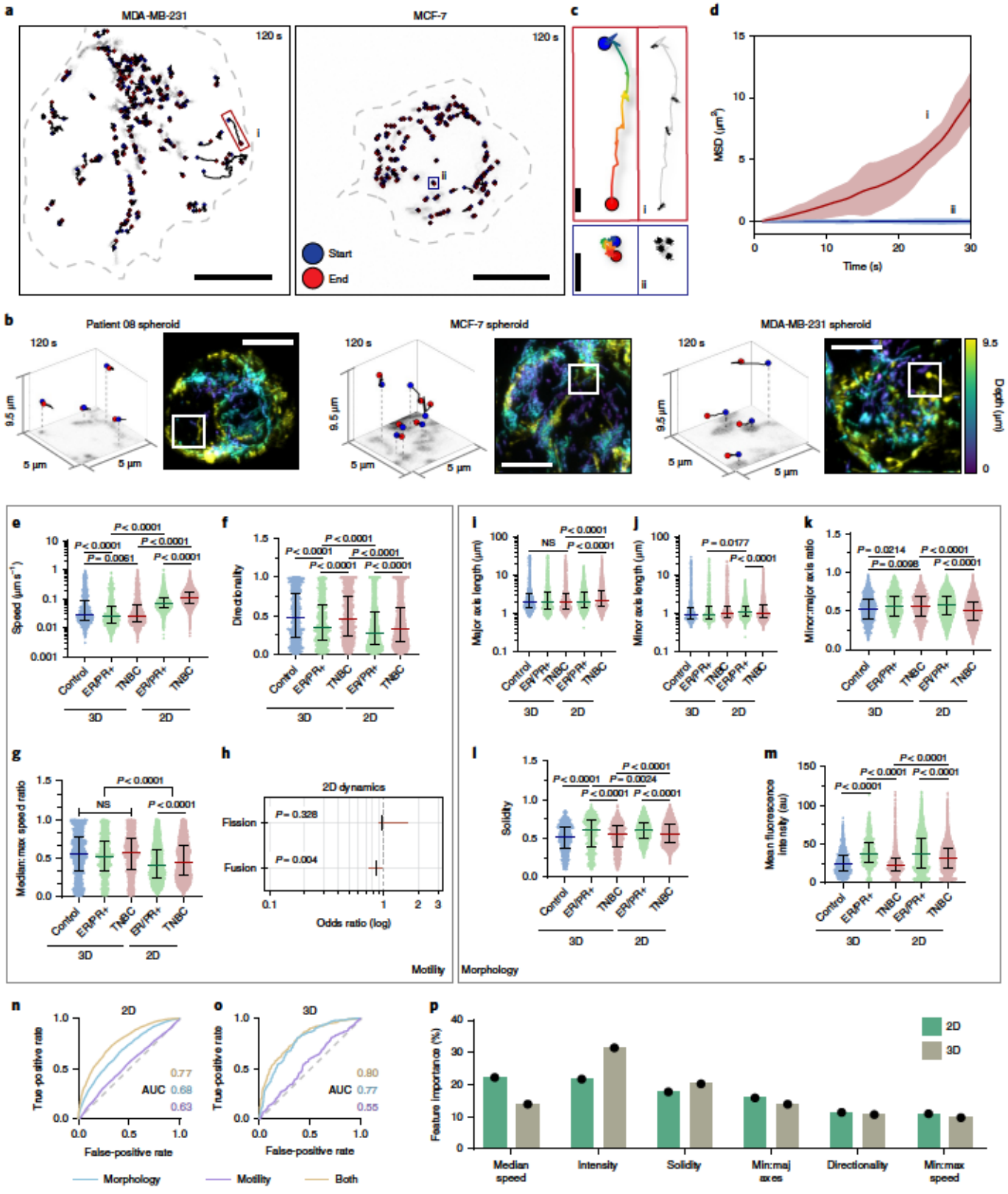

important implications for the understanding of how mitochondria are recruited to the invading edges of cells to fuel invasion and metastasis[14]. Moreover, we were able to integrate Mitometer with other fluorescence-based measurements by combining mitochondrial analysis with FLIM of NADH. Mitometer identified heterogeneity and trends in mitochondrial dynamics and morphology in relation to the bioenergetics of mitochondrial populations in varying metabolic states, which was particularly evident in breast cancer cells compared with non-cancerous mammary epithelial cells. These results suggest that specific subsets of mitochondria serve to regulate tumorigenic metabolism, and will lead to important insights into how these organelles drive tumor progression. This study critically depended on object-based tracking to quantify NADH lifetime values of individual mitochondria instead of individual pixels in an averaged fluorescence image stack. Additionally, Mitometer's ability to build tracks with accurate track lifetimes allowed sufficient FLIM

Fig. 6 | Cancer-specific metabolic heterogeneity in single mitochondria. a, TMRM-labeled mitochondria overlaid with a pseudocolor corresponding to the mean fraction of bound NADH. Scale bars, 20 µm. Shown are six different breast cell lines in three different subcategories: normal breast epithelial cells (blue), cancerous and receptor-positive (ER/PR+) breast cells (green) and TNBC cells (red). **b**, Histogram distributions of the mitochondrial fraction of bound NADH of normal, ER/PR+ and TNBC cells. **c**, The mean fraction of bound NADH of each cell type's mitochondria. **d**, The coefficients of variation of bound NADH for each cell type. $n = 13$, 21 and 28 distinct cells (**c**,**d**). **e**, Spearman's correlation coefficient (r) between bound NADH and the mitochondrial parameters of motility and morphology for each cell type. **f**–**l**, Normalized fraction of NADHb in control (gray) and antimycin A (AA)-treated (orange) cells (**f**), along with the median speed (**g**), mean speed (**h**), maximum speed (**i**), solidity (**j**), directionality (**k**) and mean fluorescence intensity (**l**) of control and AA-treated mitochondria. $n = 852$, 1,634 and 1,958 distinct mitochondrial tracks in normal, ER/PR+ and TNBC samples, respectively (**b**,**e**); $n = 19$, 10 distinct cells in control and AA conditions, respectively (**f**); $n = 2{,}470$, 1,586 distinct mitochondria in control and AA conditions, respectively (**g**–**l**). Data are given as the mean ± s.e.m. (**c**,**d**,**f**) or median ± interquartile ranges (**g**–**l**). ±P values are calculated using the Kruskal–Wallis non-parametric rank test with a post-hoc Dunn's multiple comparison test ($H = 14.50$, 17.62) (**c**,**d**,**g**–**l**), a Spearman's two-tailed rank correlation test (**e**) or a Student's two-tailed t-test (**f**).

data to be averaged through the image stack for each mitochondrion to reliably quantify its fraction of bound NADH.

We hope Mitometer will encourage the widespread dissemination of mitochondrial morphological and motility feature datasets, which would allow the use of deep learning techniques to improve unbiased and situation-specific segmentation and tracking. Additionally, Mitometer currently requires a time-lapse image for automated segmentation, which presumably can be overcome with data-driven machine learning techniques and would be advantageous for morphology-only analyses.

This pipeline, which features a simple and intuitive user interface and ImageJ compatibility, is accessible to any cell biologist with the ability to acquire fluorescence images. Mitometer may be adapted to a variety of other applications for which segmentation and tracking of variably sized objects in a noisy image is required, including but not limited to other organelles and intracellular structures. The further integration of Mitometer with other mitochondria-localizing probes, such as intracellular oxygen sensors[53], temperature sensors[54] and pH sensors[55], opens the door to many additional exciting avenues for the investigation of biologic and, more specifically, metabolic alterations at the level of the single mitochondrion in live cells and animal models.

Online content

Any methods, additional references, Nature Research reporting summaries, source data, extended data, supplementary information, acknowledgements, peer review information; details of author contributions and competing interests; and statements of data and code availability are available at https://doi.org/10.1038/s41592-021-01234-z.

Received: 3 November 2020; Accepted: 6 July 2021;
Published online: 19 August 2021

References

1. Iwata, R., Casimir, P. & Vanderhaeghen, P. Mitochondrial dynamics in postmitotic cells regulate neurogenesis. *Science* **369**, 858–862 (2020).
2. Federico, A. et al. Mitochondria, oxidative stress and neurodegeneration. *J. Neurol. Sci.* **322**, 254–262 (2012).
3. Green, D. R. & Reed, J. C. Mitochondria and apoptosis. *Science* **281**, 1309–1312 (1998).
4. Schiavon, C. R. et al. Actin chromobody imaging reveals sub-organellar actin dynamics. *Nat. Methods* **17**, 917–921 (2020).
5. Baloh, R. H. Mitochondrial dynamics and peripheral neuropathy. *Neuroscientist* **14**, 12–18 (2008).
6. Westermann, B. Mitochondrial fusion and fission in cell life and death. *Nat. Rev. Mol. Cell Biol.* **11**, 872–884 (2010).
7. Pigino, G. et al. Alzheimer's presenilin 1 mutations impair kinesin-based axonal transport. *J. Neurosci.* **23**, 4499–4508 (2003).
8. Rui, Y., Tiwari, P., Xie, Z. & Zheng, J. Q. Acute impairment of mitochondrial trafficking by β-amyloid peptides in hippocampal neurons. *J. Neurosci.* **26**, 10480–10487 (2006).
9. Trushina, E. et al. Mutant huntingtin impairs axonal trafficking in mammalian neurons in vivo and in vitro. *Mol. Cell. Biol.* **24**, 8195–8209 (2004).
10. Wang, X. et al. PINK1 and Parkin target Miro for phosphorylation and degradation to arrest mitochondrial motility. *Cell* **147**, 893–906 (2011).
11. Kapitein, L. C. & Hoogenraad, C. C. Building the neuronal microtubule cytoskeleton. *Neuron* **87**, 492–506 (2015).
12. Waterman-Storer, C. M. Microtubules and microscopes: how the development of light microscopic imaging technologies has contributed to discoveries about microtubule dynamics in living cells. *Mol. Biol. Cell* **9**, 3263–3271 (1998).
13. Caino, M. C. et al. Syntaphilin controls a mitochondrial rheostat for proliferation–motility decisions in cancer. *J. Clin. Invest.* **127**, 3755–3769 (2017).
14. Caino, M. C. et al. A neuronal network of mitochondrial dynamics regulates metastasis. *Nat. Commun.* **7**, 13730 (2016).
15. Cheezum, M. K., Walker, W. F. & Guilford, W. H. Quantitative comparison of algorithms for tracking single fluorescent particles. *Biophys. J.* **81**, 2378–2388 (2001).
16. Yang, Y. et al. Label-free tracking of single organelle transportation in cells with nanometer precision using a plasmonic imaging technique. *Small* **11**, 2878–2884 (2015).
17. Tinevez, J.-Y. et al. TrackMate: an open and extensible platform for single-particle tracking. *Methods* **115**, 80–90 (2017).
18. Fischer, C. A. et al. MitoSegNet: easy-to-use deep learning segmentation for analyzing mitochondrial morphology. *iScience* **23**, 101601 (2020).
19. Falk, T. et al. U-Net: deep learning for cell counting, detection, and morphometry. *Nat. Methods* **16**, 67–70 (2019).
20. Isensee, F., Jaeger, P. F., Kohl, S. A. A., Petersen, J. & Maier-Hein, K. H. nnU-Net: a self-configuring method for deep learning-based biomedical image segmentation. *Nat. Methods* **18**, 203–211 (2021).
21. Miller, K. E., Liu, X.-A. & Puthanveettil, S. V. Automated measurement of fast mitochondrial transport in neurons. *Front. Cell. Neurosci.* **9**, 435 (2015).
22. Alsina, A. et al. Real-time subpixel-accuracy tracking of single mitochondria in neurons reveals heterogeneous mitochondrial motion. *Biochem. Biophys. Res. Commun.* **493**, 776–782 (2017).
23. Vallmitjana, A., Civera-Tregon, A., Hoenicka, J., Palau, F. & Benitez, R. Motion estimation of subcellular structures from fluorescence microscopy images. *Annu. Int. Conf. IEEE Eng. Med. Biol. Soc.* **2017**, 4419–4422 (2017).
24. Winter, M. R., Fang, C., Banker, G., Roysam, B. & Cohen, A. R. Axonal transport analysis using multitemporal association tracking. *Int. J. Comput. Biol. Drug Des.* **5**, 35–48 (2012).
25. Kandel, J., Chou, P. & Eckmann, D. M. Automated detection of whole-cell mitochondrial motility and its dependence on cytoarchitectural integrity. *Biotechnol. Bioeng.* **112**, 1395–1405 (2015).
26. Giedt, R. J., Pfeiffer, D. R., Matzavinos, A., Kao, C.-Y. & Alevriadou, B. R. Mitochondrial dynamics and motility inside living vascular endothelial cells: role of bioenergetics. *Ann. Biomed. Eng.* **40**, 1903–1916 (2012).
27. Valente, A. J., Maddalena, L. A., Robb, E. L., Moradi, F. & Stuart, J. A. A simple ImageJ macro tool for analyzing mitochondrial network morphology in mammalian cell culture. *Acta Histochem.* **119**, 315–326 (2017).
28. Viana, M. P., Lim, S. & Rafelski, S. M. Quantifying mitochondrial content in living cells. *Methods Cell Biol.* **125**, 77–93 (2015).
29. Lihavainen, E., Mäkelä, J., Spelbrink, J. N. & Ribeiro, A. S. Mytoe: automatic analysis of mitochondrial dynamics. *Bioinformatics* **28**, 1050–1051 (2012).
30. Klopfenstein, D. R. & Vale, R. D. The lipid binding pleckstrin homology domain in UNC-104 kinesin is necessary for synaptic vesicle transport in *Caenorhabditis elegans*. *Mol. Biol. Cell* **15**, 3729–3739 (2004).
31. Pilling, A. D., Horiuchi, D., Lively, C. M. & Saxton, W. M. Kinesin-1 and Dynein are the primary motors for fast transport of mitochondria in *Drosophila* motor axons. *Mol. Biol. Cell* **17**, 2057–2068 (2006).
32. Chang, C.-R. & Blackstone, C. Dynamic regulation of mitochondrial fission through modification of the dynamin-related protein Drp1. *Ann. NY Acad. Sci.* **1201**, 34–39 (2010).
33. Ploumi, C., Daskalaki, I. & Tavernarakis, N. Mitochondrial biogenesis and clearance: a balancing act. *FEBS J.* **284**, 183–195 (2017).
34. McCarron, J. G. et al. From structure to function: mitochondrial morphology, motion and shaping in vascular smooth muscle. *J. Vasc. Res.* **50**, 357–371 (2013).

35. Smal, I., Draegestein, K., Galjart, N., Niessen, W. & Meijering, E. Particle filtering for multiple object tracking in dynamic fluorescence microscopy images: application to microtubule growth analysis. *IEEE Trans. Med. Imaging* **27**, 789–804 (2008).
36. Dorn, J. F., Danuser, G. & Yang, G. Computational processing and analysis of dynamic fluorescence image data. *Methods Cell Biol.* **85**, 497–538 (2008).
37. Huth, J. et al. Significantly improved precision of cell migration analysis in time-lapse video microscopy through use of a fully automated tracking system. *BMC Cell Biol.* **11**, 24 (2010).
38. Vasquez, R. J., Howell, B., Yvon, A. M., Wadsworth, P. & Cassimeris, L. Nanomolar concentrations of nocodazole alter microtubule dynamic instability in vivo and in vitro. *Mol. Biol. Cell* **8**, 973–985 (1997).
39. Heggeness, M. H., Simon, M. & Singer, S. J. Association of mitochondria with microtubules in cultured cells. *Proc. Natl Acad. Sci. USA* **75**, 3863–3866 (1978).
40. Rambold, A. S., Kostelecky, B., Elia, N. & Lippincott-Schwartz, J. Tubular network formation protects mitochondria from autophagosomal degradation during nutrient starvation. *Proc. Natl Acad. Sci. USA* **108**, 10190–10195 (2011).
41. Leonard, A. P. et al. Quantitative analysis of mitochondrial morphology and membrane potential in living cells using high-content imaging, machine learning, and morphological binning. *Biochim. Biophys. Acta* **1853**, 348–360 (2015).
42. Gomes, L. C., Di Benedetto, G. & Scorrano, L. During autophagy mitochondria elongate, are spared from degradation and sustain cell viability. *Nat. Cell Biol.* **13**, 589–598 (2011).
43. DeRose, Y. S. et al. Tumor grafts derived from women with breast cancer authentically reflect tumor pathology, growth, metastasis and disease outcomes. *Nat. Med.* **17**, 1514–1520 (2011).
44. Ma, D. et al. Patient-derived xenograft culture-transplant system for investigation of human breast cancer metastasis. Preprint at *bioRxiv* https://doi.org/10.1101/2020.06.25.172056 (2020).
45. Wu, P.-H., Giri, A., Sun, S. X. & Wirtz, D. Three-dimensional cell migration does not follow a random walk. *Proc. Natl Acad. Sci. USA* **111**, 3949–3954 (2014).
46. Zhao, J. et al. Mitochondrial dynamics regulates migration and invasion of breast cancer cells. *Oncogene* **32**, 4814–4824 (2013).
47. Walker, J. E. The ATP synthase: the understood, the uncertain and the unknown. *Biochem. Soc. Trans.* **41**, 1–16 (2013).
48. Pedregosa, F. et al. Scikit-learn: machine learning in Python. *J. Mach. Learn. Res.* **12**, 2825–2830 (2011).
49. Digman, M. A., Caiolfa, V. R., Zamai, M. & Gratton, E. The phasor approach to fluorescence lifetime imaging analysis. *Biophys. J.* **94**, L14–L16 (2008).
50. Bird, D. K. et al. Metabolic mapping of MCF10A human breast cells via multiphoton fluorescence lifetime imaging of the coenzyme NADH. *Cancer Res.* **65**, 8766–8773 (2005).
51. Stringari, C. et al. Phasor approach to fluorescence lifetime microscopy distinguishes different metabolic states of germ cells in a live tissue. *Proc. Natl Acad. Sci. USA* **108**, 13582–13587 (2011).
52. Scaduto, R. C. & Grotyohann, L. W. Measurement of mitochondrial membrane potential using fluorescent rhodamine derivatives. *Biophys. J.* **76**, 469–477 (1999).
53. Will, Y., Hynes, J., Ogurtsov, V. I. & Papkovsky, D. B. Analysis of mitochondrial function using phosphorescent oxygen-sensitive probes. *Nat. Protoc.* **1**, 2563–2572 (2006).
54. Arai, S. et al. Mitochondria-targeted fluorescent thermometer monitors intracellular temperature gradient. *Chem. Commun. (Camb.)* **51**, 8044–8047 (2015).
55. Lee, M. H. et al. Mitochondria-immobilized pH-sensitive off–on fluorescent probe. *J. Am. Chem. Soc.* **136**, 14136–14142 (2014).

Methods

Primary human mammary tissue dissociation and processing. Human reduction mammoplasty samples were obtained with informed consent through the Cooperative Human Tissue Network (CHTN) under the approved institutional review board protocol UCI 17-05. Tissue samples were processed as previously reported[56]. In brief, human mammary tissues were washed in PBS, mechanically dissociated with scalpels, digested with 2 mg ml^{-1} collagenase type I (Life Technologies, 17100-017) in DMEM with 5% FBS at 37 °C overnight on a shaker, treated with DNase I (Worthington Biochemical, LS002139) and subjected to three pulse centrifugations to 500×*g*. Supernatants were then collected and centrifuged for 5 min at 500×*g* to isolate primary mammary fibroblasts, and pellets containing mammary epithelial organoids were digested with trypsin (Corning, 25-052-CI) for 10 min at 37 °C to generate single-cell suspensions of primary mammary epithelial cells. Cells were filtered through a 70 µm strainer.

Collection and processing of PDX tumors. All tissue samples were collected with informed consent from individuals being treated at the Huntsman Cancer Hospital and the University of Utah. Samples were collected and de-identified by the Huntsman Cancer Institute Tissue Resource and Application Core facility before being obtained for implantation under a protocol approved by the University of Utah Institutional Review Board. We were able to obtain human reduction mammoplasty samples under the approved institutional review board protocol UCI 17-05. HCI-010 and HCI-002 PDX tumors[45] were established and grown in NSG mice purchased from The Jackson Laboratory. Animals were maintained in a pathogen-free facility and animal procedures were approved by the University of California, Irvine, Institutional Animal Care and Use Committee. After 3–6 months of growth, PDX tumors were collected, mechanically dissociated, digested with 2 mg ml^{-1} collagenase type IV (Sigma-Aldrich, C5138-1G) in DMEM with 5% FBS at 37 °C for 45 min on a shaker. Digested tumors were washed with PBS, treated with DNase I (Worthington Biochemical, LS002139) and dissociated to single cells with trypsin (Corning, 25-052-CI). PDX cells were filtered through a 70 µm strainer.

Primary and PDX cell culture. Primary mammary epithelial cells and HCI-010 and HCI-002 PDX cells were grown in 3D spheroid culture as previously described[44]. In brief, approximately 7×10^4–1×10^5 cells were embedded in Corning Matrigel Growth Factor Reduced Matrix (Corning, 354230) and cultured on 35 mm glass-bottom imaging dishes in EpiCult Medium (StemCell Technologies, 05610) supplemented with 5% FBS, 10 ng ml^{-1} human epidermal growth factor (PeproTech, AF-100-15), 10 ng ml^{-1} basic fibroblast growth factor (PeproTech, 100-18B) and 1% penicillin–streptomycin (Hyclone, SV30010) for 4–7 d at 37 °C at 5% CO_2 before imaging.

Three-dimensional culture of cell lines. Cell lines were embedded in Corning Matrigel Growth Factor Reduced Matrix (Corning, 354230) using seeding densities of between 5×10^4 and 1×10^5 cells. Embedded cells were grown in 3D spheroid culture on 35 mm glass-bottom imaging dishes in DMEM supplemented with 10% FBS and 1% penicillin–streptomycin (Hyclone, SV30010) for 4–7 d at 37 °C at 5% CO_2 before imaging.

Two-dimensional culture of cell lines. Cell lines were plated on 10 µg ml^{-1} fibronectin-coated 35 mm glass-bottom imaging dishes in DMEM supplemented with 10% FBS and 1% penicillin–streptomycin (Hyclone, SV30010) or, in the case of MCF-10A cells, DMEM/F12 media supplemented with 5% horse serum, 20 ng µl^{-1} epidermal growth factor (PeproTech, AF-100-15), 0.5 mg ml^{-1} hydrocortisone (Sigma, H0888), 100 ng ml^{-1} cholera toxin (Sigma, C8052), 10 µg ml^{-1} insulin (Sigma, I1882) and 1% penicillin–streptomycin (Hyclone, SV30010) at 37 °C at 5% CO_2 before imaging.

TMRM studies. For TMRM experiments, 2D and 3D cell cultures in imaging dishes were incubated with 100 nM TMRM for 15 min without washout, immediately followed by imaging.

Nocodazole studies. For in vitro nocodazole validation studies, 100 nM TMRM was added to cells for 45 min, followed by the addition of nocodazole at a final concentration of 10 µM. The treatment was applied for 1 h without washout, immediately followed by imaging.

Fission and fusion studies. Cells were first treated with 100 nM TMRM for 45 min, and immediately imaged for 1 min time lapses at 15 min intervals for 40 min. To induce mitochondrial fission, 10 µM oligomycin was added to the medium. To induce mitochondrial fusion, the media was replaced with phenol red-free HBSS with 10 mM HEPES. Cells were then again imaged for 1 min time lapses at 15 min intervals for 140 min.

Mitochondria and fluorescence lifetime imaging. For nocodazole and MEF fission and fusion studies we performed experiments on an LSM 880 (Zeiss), and for HeLa fission and fusion studies on an LSM 710 (Zeiss) inverted laser scanning confocal microscope with a 63×, numerical aperture 1.4, oil-immersion objective, at a frame size of 512× 512 pixels, with a pixel size of 138 nm, and at a rate of 1 frame per second for 30 s.

For 2D and 3D TMRM studies we performed experiments on a Zeiss LSM 710 inverted laser scanning confocal microscope with a 40×, numerical aperture 1.2 water-immersion objective. In the 2D studies we used a frame size of 512× 512 with a pixel size of 87.9 nm and at a rate of 1 frame per second for 120 frames. In the 3D studies we used a frame size of 256 × 256 with a pixel size of 105.4 nm and at a rate of 1 stack every 10 s, with 21 *z*-planes per stack at a distance of 450 nm between planes. In both cases, we used a two-photon titanium : sapphire laser (Spectra-Physics, MaiTai) to excite the TMRM at a wavelength of 820 nm, which was passed through a 690 nm dichroic filter. The fluorescence emission in the range of 520–700 nm was captured through the microscope's internal detector. The cells were kept under biological conditions through the imaging. Images were converted to TIFs in ImageJ v1.53c.

For FLIM of NADH studies, we performed experiments on a Zeiss LSM 710 inverted laser scanning confocal microscope with a 63×, numerical aperture 1.4, oil-immersion objective at a frame size of 256 × 256 with a pixel size of 180 nm and at a rate of 0.398 frames per second for varying numbers of frames. The cells were excited at approximately 2 mW at the plane of excitation with a two-photon titanium : sapphire laser (Spectra-Physics, MaiTai) at 740 nm, which was passed through a 690 nm dichroic filter. The fluorescence emission was separated through two bandpass filters, a 460/80 nm filter for NADH fluorescence emission and a 641/75 nm filter for TMRM fluorescence emission, and was then detected using two separate photomultiplier tubes (Hamamatsu, H7422P-40). The fluorescence lifetime decays were captured in the frequency domain via an A320 FastFLIM box (ISS) and calibrated using SimFCS v4 developed at the Laboratory for Fluorescence Dynamics at the University of California, Irvine. Coumarin-6 in ethanol, with a known single exponential fluorescence lifetime of 2.5 ns, was imaged on each day of imaging and was used as the calibration sample for the instrument response time. The cells were kept under biological conditions through the imaging.

Statistical testing. Random forest classification was implemented using the scikit-learn package in Python. All other statistical analyses were done using Graphpad Prism v7.

Reporting Summary. Further information on research design is available in the Nature Research Reporting Summary linked to this article.

Data availability

The authors declare that all data supporting the findings of this study are available in the article and its supplementary information files or from the corresponding author upon reasonable request. Source data are provided with this paper.

Code availability

The Mitometer program is written in MATLAB (MathWorks). The MATLAB GUI Mitometer app and corresponding source code are available as Supplementary Software. The software and updated versions are also freely available online through GitHub at https://github.com/aelefebv/Mitometer, with a direct download link available at https://github.com/aelefebv/Mitometer/archive/refs/heads/main.zip.

References

56. Nguyen, Q. H. et al. Profiling human breast epithelial cells using single cell RNA sequencing identifies cell diversity. *Nat. Commun.* **9**, 2028 (2018).

Acknowledgements

The authors thank F. Adame and M. Li for much of the cell culture work, and F. Palomba, A. Vallmitjana and L. Scipioni for thoughtful feedback on experimental design and careful review of the manuscript. The authors also thank E. Gratton for helpful discussions and advice on the application of Mitometer to metabolic analysis of single mitochondria; G. A. Hernandez for her technical assistance with processing human mammary samples for this project; and A. Welm at the Huntsman Cancer Institute, Salt Lake City, Utah for generously providing PDX models used in this study. R. Waymack from the laboratory of Z. Wunderlich at University of California, Irvine is thanked for the help on imaging with the Nikon Eclipse Ti-E. Image and data acquisition were made possible through access to the Laboratory for Fluorescence Dynamics, a shared resource center supported by the National Institutes of Health (grant no. P41-GM103540). This study was supported by funds from the National Science Foundation (grant nos. DMS1763272 and 1847005 to M.A.D. and NSF GRFP DGE-1839285 to A.E.Y.T.L.), a grant from the Simons Foundation (594598 QN), by funds from the National Institutes of Health and the National Cancer Institute (1R01CA234496 to K.K.; K22 CA190511 to D.A.L.), the American Cancer Society (132551-RSG-18-194-01-DDC to K.K.), and the V Foundation (V2019-019 to D.A.L.). D.M. was supported by the Canadian Institutes of Health Research Postdoctoral Fellowship.

Author contributions

A.E.Y.T.L. initiated the study, designed and implemented the Mitometer software, designed and performed cellular imaging experiments and analysis, and wrote the manuscript. D.M. designed the experiments, prepared and cultured the 3D primary samples and cell lines for the breast cancer and non-malignant breast cell experiments, and extensively reviewed and edited the manuscript. K.K. and D.A.L. helped review and edit the manuscript. M.A.D. initiated the study, supervised the research, and helped review and edit the manuscript.

Competing interests

The authors declare no competing interests.

Additional information

Extended data are available for this paper at https://doi.org/10.1038/s41592-021-01234-z.

Supplementary information The online version contains supplementary material available at https://doi.org/10.1038/s41592-021-01234-z.

Correspondence and requests for materials should be addressed to M.A.D.

Peer review information *Nature Methods* thanks Carsten Marr and the other, anonymous, reviewer(s) for their contribution to the peer review of this work. Rita Strack was the primary editor on this article and managed its editorial process and peer review in collaboration with the rest of the editorial team.

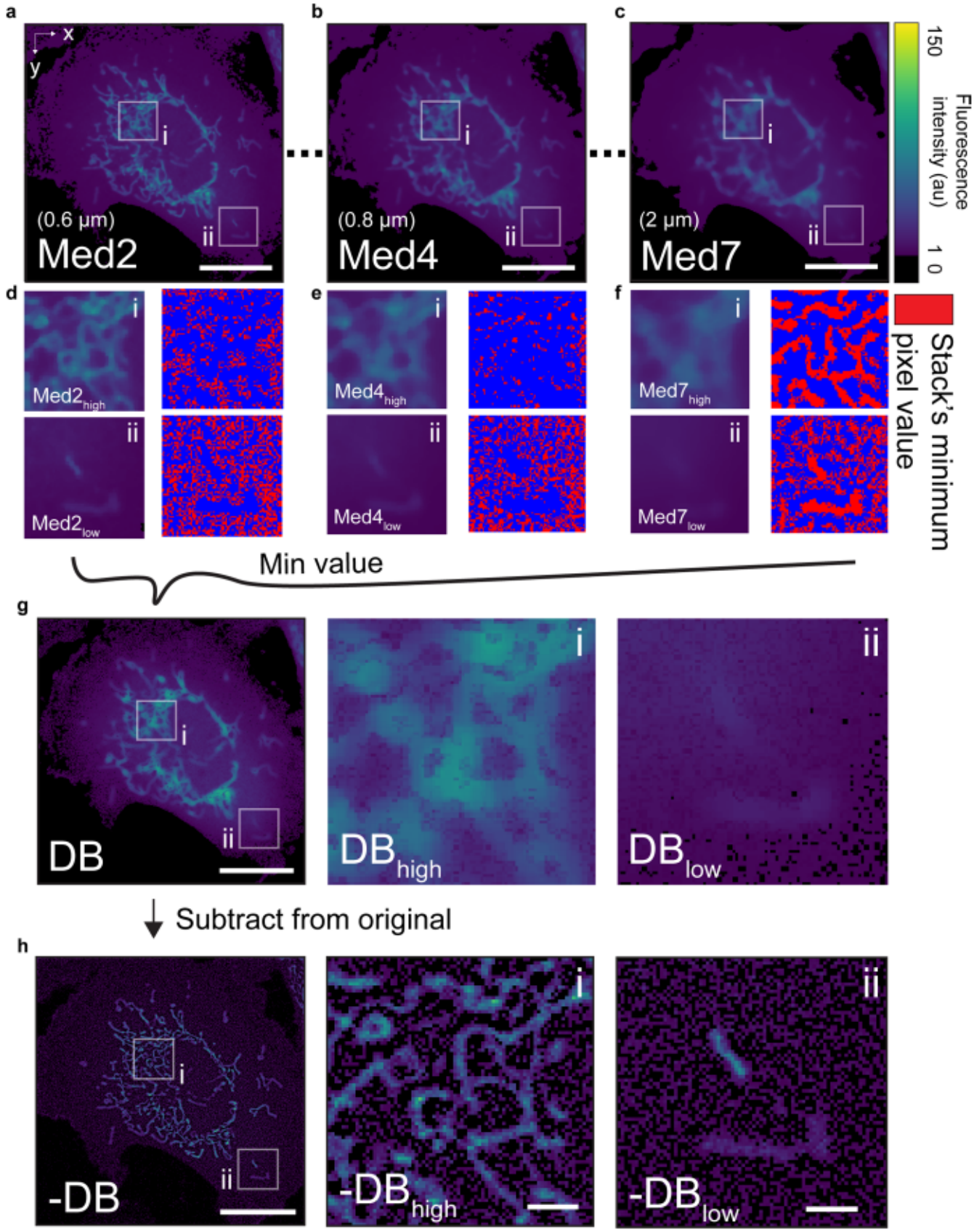

Extended Data Fig. 1 | See next page for caption.

Extended Data Fig. 1 | Diffuse background removal surrounding objects of complex shapes. Circular median filters of diameters of 0.6 μm (**a**) to 2 μm (**c**) (corresponding to the minimum area threshold and a value larger than the minor axis length of mitochondria) in 1-pixel increments (**b**) are convolved with the original image. Close-ups of regions with high (i) and low (i) diffuse background noise convolved with a small (**d**) medium (**e**) and large (**f**) median filter (left), with corresponding minimum median filter values at each filter size (right). **g**, The minimum value of each pixel in the stack of median filtered images (which also contains the original image) is used to build the diffuse background image, showing high diffuse noise in the dense regions (i) and minimal diffuse noise in the sparse regions (ii). **h**, The diffuse background image is then subtracted from the original image to produce a diffuse background subtracted image, separating adjacent mitochondria in dense regions (i) and keeping mitochondria intact in sparse regions (ii).

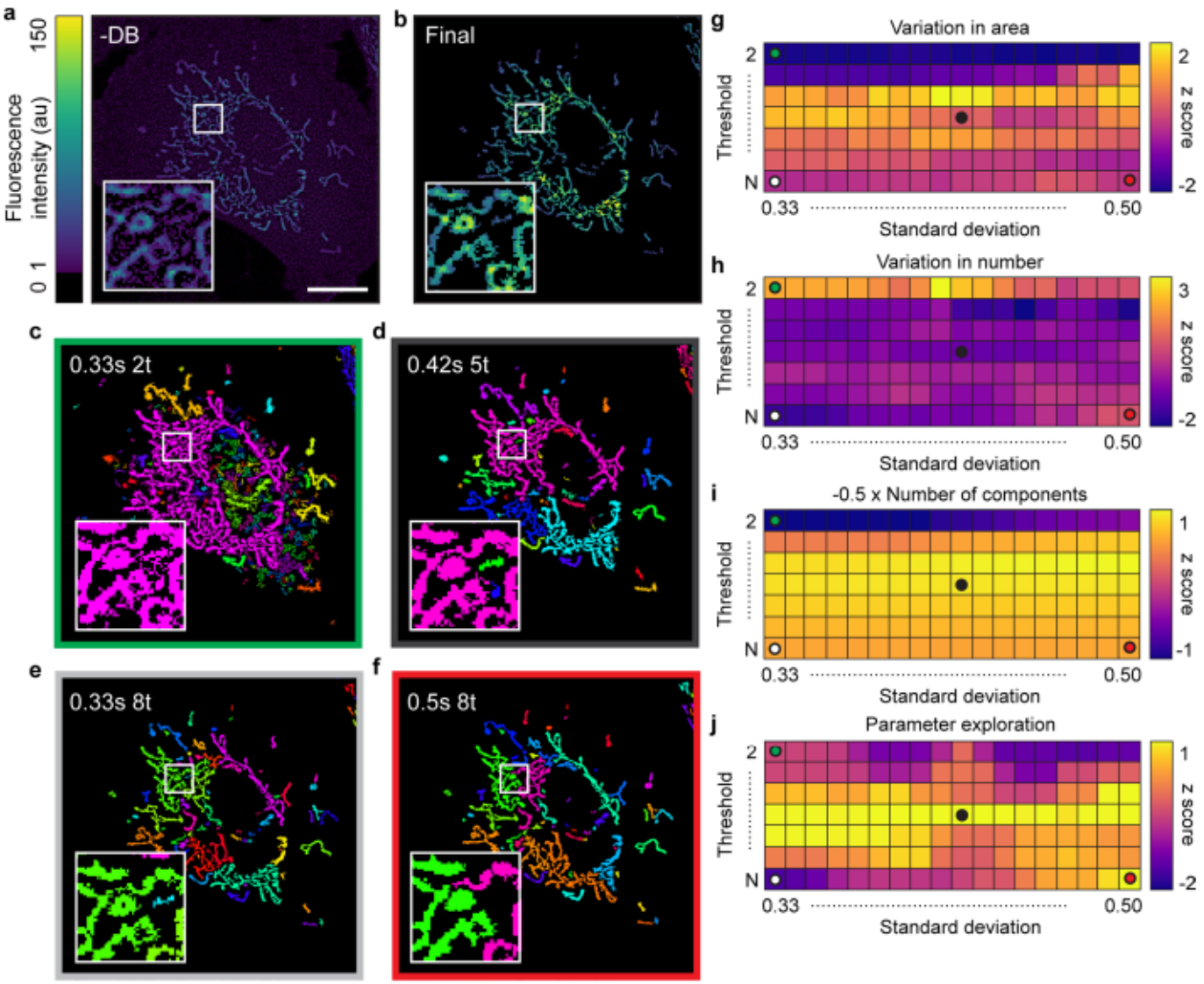

Extended Data Fig. 2 | Parameter exploration for choosing low-pass filter and threshold parameters. a, The diffuse background subtracted (-DB) image is taken as an input. **b**, The output is an image with optimal parameters (**e**) chosen to segment mitochondrial objects and remove noise. A mismatch in parameters results in high noise (**c**), false connections and area overestimation (**d**), and loose connections (leading to high variability) with area overestimation (**f**). The parameters are chosen based on the z score normalized addition of 3 features: the variability in the median area of the mitochondria between temporal frames (**g**), the variability in the number of mitochondria found between temporal frames (**h**), and ½ the negative number of mitochondria found between temporal frames (**I**). We give less weight to the number of mitochondria found as many false disconnections biases the parameter selection towards a highly thresholded image, while noise biases the parameter selection towards a non-thresholded image. This addition results in the cost function used for minimization to select optimal parameters, which we run through a symmetrically padded 3×3 median filter to ensure selected parameters are in a region of low cost, rather than an outlying point (**J**). Colored dots represent parameters chosen to create images shown in **c-f** with respective border colors. Colors in **c-f** represent randomly pseudocolored connected components.

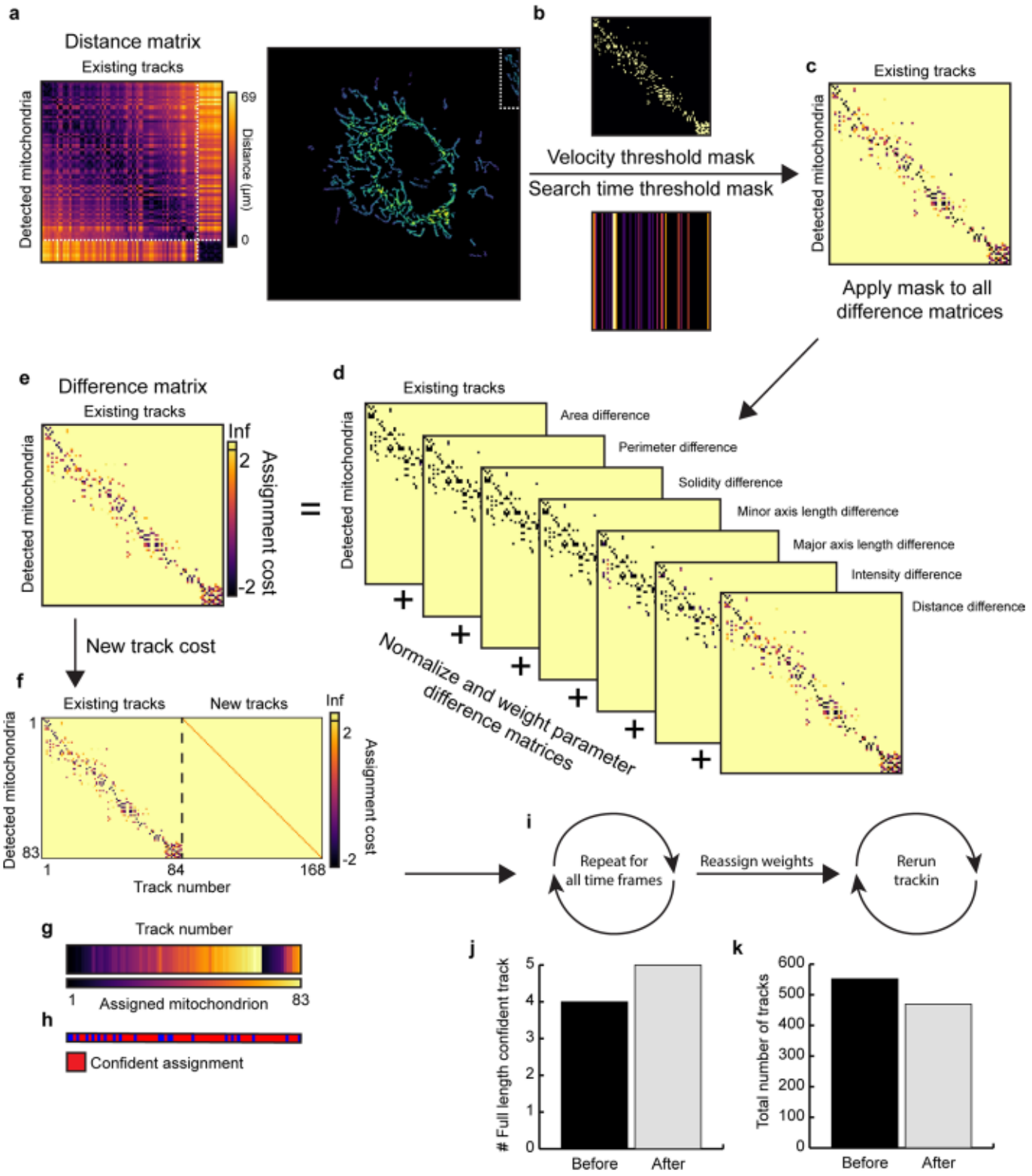

Extended Data Fig. 3 | See next page for caption.

Extended Data Fig. 3 | Flowchart for morphology and displacement-based global cost minimization tracking. a, A matrix of intensity weighted centroid distances is built comprised of the difference between every existing track (columns) and every mitochondrion found in the current time frame (rows). A region of mitochondria from an adjacent cell can be seen in the dotted white area, resulting in large differences between the mitochondria of the two cells. **b**, A mask is created to avoid assignments between any mitochondria and track which are further than 3 frames apart (the maximum search time threshold), and at a distance greater than 1 μm multiplied by the frame time apart (the maximum velocity threshold). **c**, The mask is applied to the difference matrices of all mitochondrial features and distance. **d**, The difference matrices are then squared, z score normalized, weighted, and summed to create the final difference matrix (**e**). **f**, A diagonal matrix of new track costs is appended to the difference matrix to allow newly found mitochondria to be assigned to a new track. **g**, Every mitochondrion (row) in the matrix is assigned to a single track (column) that leads to a globally minimized cost of assignment. **h**, A mitochondrion which is assigned to a track that also corresponds to its own individually minimum cost is labelled as a confident assignment. **I**, This process is repeated for all temporal frames. All confident tracks are then analyzed for interCoV:intraCoV ratios for each mitochondrial morphological feature, and weights are set accordingly. These weights are used to rerun the tracking algorithm, leading to a higher number of mitochondria that are confidently tracked for the full length of the time stack (**j**) and to less total number of tracks overall (**k**).

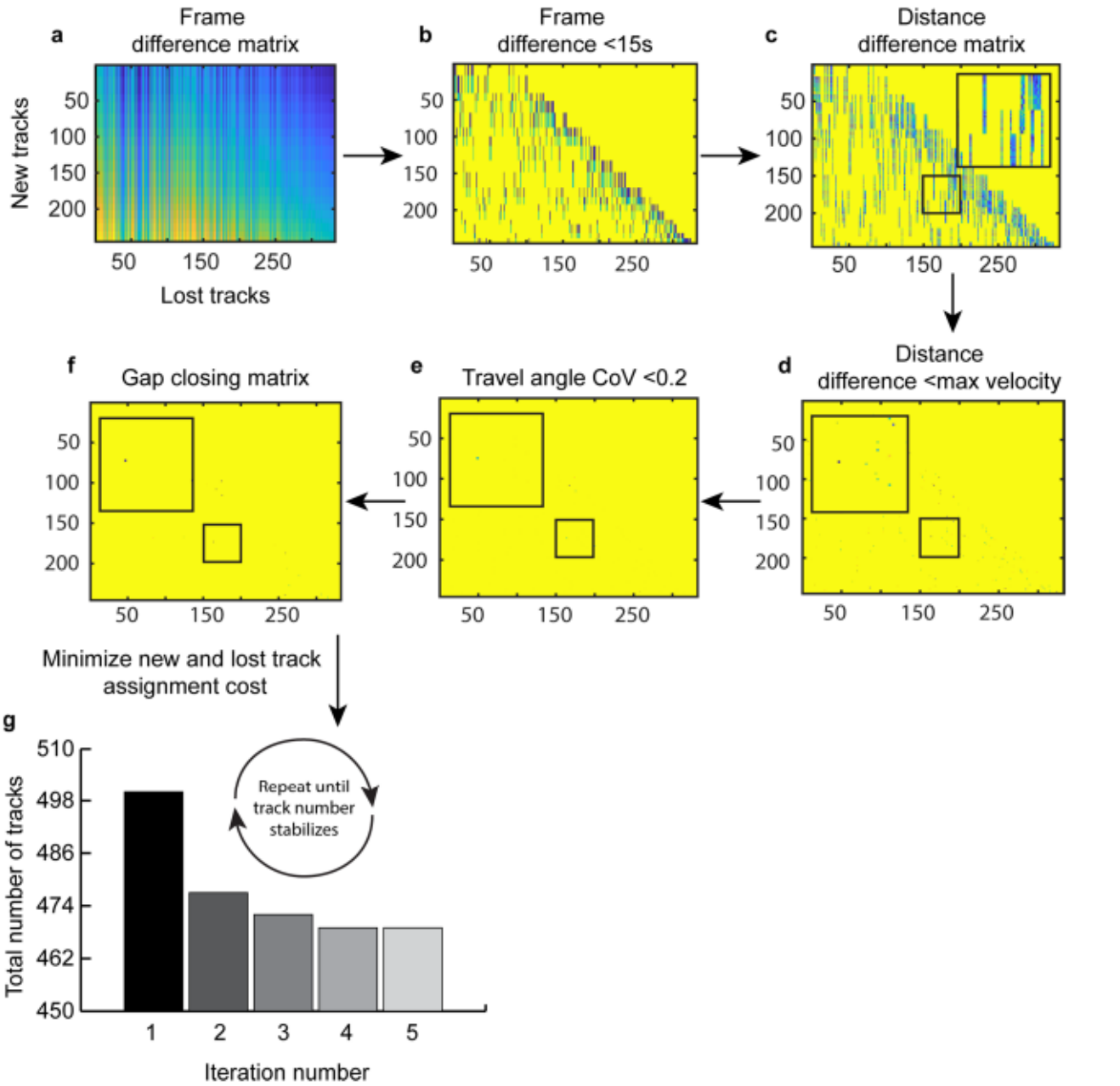

Extended Data Fig. 4 | Flowchart for gap-closing scheme. a, A matrix of differences between all new tracks' first frame number and all lost tracks' last frame number. **b**, The frame difference matrix is thresholded based a maximum search time threshold of 15 seconds to create a mask. **c**, The mask is applied to the matrix of the intensity weighted centroid distances between the new tracks' first centroid position and last tracks' last centroid position. **d**, The distance matrix is thresholded based on the maximum velocity threshold of 1 μm/s. **e**, Any gap closure resulting in a travel angle coefficient of variation under 0.2 is removed. **f**, The final masked gap closing matrix is produced, which is then globally minimized to assign new tracks with possible lost track candidates. **g**, The gap-closing scheme is repeated in its entirety until the total number of tracks stabilizes. In this example, it took 4 iterations to stabilize to 469 tracks.

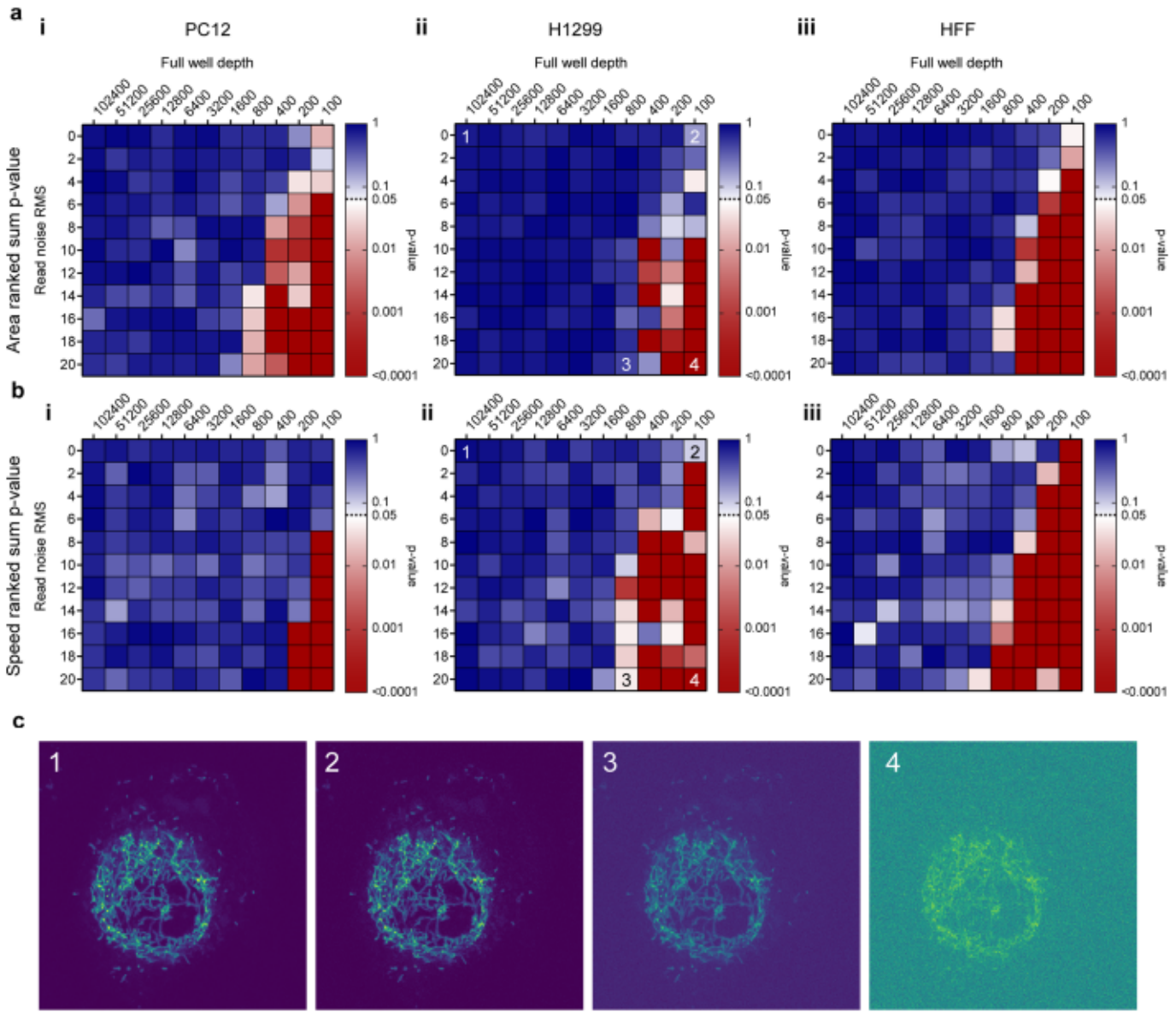

Extended Data Fig. 5 | Live-cell time lapse images with added noise. The comparison of area (**a**) and speed (**b**) of mitochondria in live-cell time lapse images of PC12 (**i**), H1299 (**ii**), and HFF (**iii**) cells between the original image and images with added noise to simulate a lower full well depth (Poissonian noise) and higher read noise root mean square (RMS) value (Gaussian noise). Comparisons are done via a two-sided Wilcoxon rank sum test. **c**, Representative images of TMRM labelled H1299 cells with simulated noise corresponding to the numbers in panels **ii**. N = 3 time lapse images per cell line.

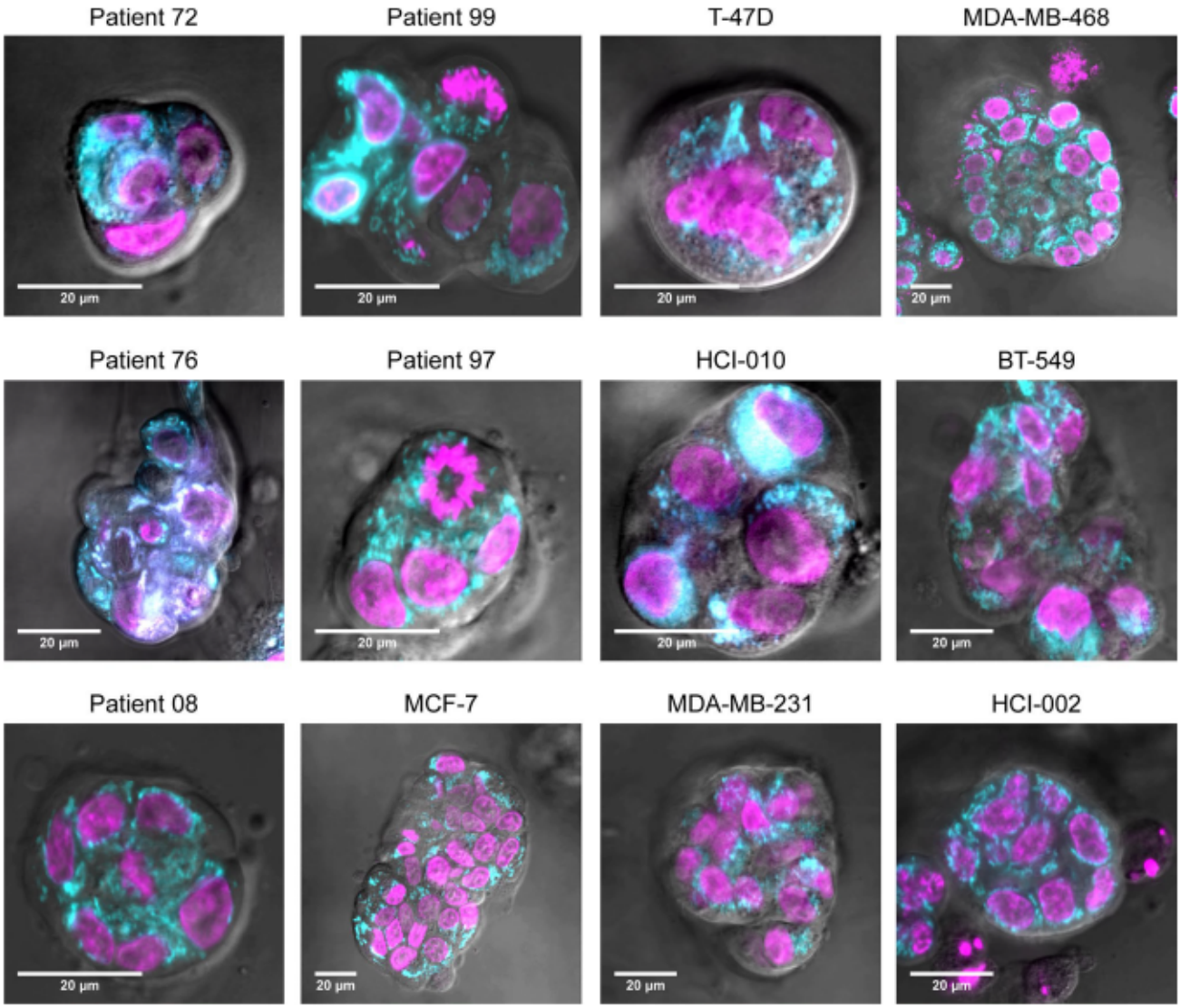

Extended Data Fig. 6 | Three-dimensional spheroid cultures. a Representative images of human reduction mammoplasty samples (Patient 72, Patient 76, Patient 08, Patient 99, Patient 97), established breast cancer cell lines (MCF-7, T-47D, MDA-MB-231, MDA-MB-468, BT-549), and patient derived xenografts (HCI-010, HCI-002) embedded in Matrigel and grown in three-dimensional spheroid culture. Gray = brightfield, cyan = mitochondria fluorescence (TMRM), pink = nuclear fluorescence (NucBlue).

nature research

Corresponding author(s): Dr. Michelle A. Digman

Last updated by author(s): Jun 21, 2021

Reporting Summary

Nature Research wishes to improve the reproducibility of the work that we publish. This form provides structure for consistency and transparency in reporting. For further information on Nature Research policies, see our Editorial Policies and the Editorial Policy Checklist.

Statistics

For all statistical analyses, confirm that the following items are present in the figure legend, table legend, main text, or Methods section.

n/a	Confirmed	
☐	☒	The exact sample size (*n*) for each experimental group/condition, given as a discrete number and unit of measurement
☐	☒	A statement on whether measurements were taken from distinct samples or whether the same sample was measured repeatedly
☐	☒	The statistical test(s) used AND whether they are one- or two-sided *Only common tests should be described solely by name; describe more complex techniques in the Methods section.*
☐	☒	A description of all covariates tested
☐	☒	A description of any assumptions or corrections, such as tests of normality and adjustment for multiple comparisons
☐	☒	A full description of the statistical parameters including central tendency (e.g. means) or other basic estimates (e.g. regression coefficient) AND variation (e.g. standard deviation) or associated estimates of uncertainty (e.g. confidence intervals)
☐	☒	For null hypothesis testing, the test statistic (e.g. *F*, *t*, *r*) with confidence intervals, effect sizes, degrees of freedom and *P* value noted *Give P values as exact values whenever suitable.*
☒	☐	For Bayesian analysis, information on the choice of priors and Markov chain Monte Carlo settings
☒	☐	For hierarchical and complex designs, identification of the appropriate level for tests and full reporting of outcomes
☐	☒	Estimates of effect sizes (e.g. Cohen's *d*, Pearson's *r*), indicating how they were calculated

Our web collection on statistics for biologists contains articles on many of the points above.

Software and code

Policy information about availability of computer code

Data collection	All mitochondrial segmentation and tracking codes are available at https://github.com/aelefebv/Mitometer. All additional codes for simulating mitochondria and their motion are available at https://github.com/aelefebv/Mitometer-Supplement. FLIM data was collected through the SimFCS version 4 software (https://www.lfd.uci.edu/globals/).
Data analysis	All additional codes used in this manuscript for analyzing mitochondrial dynamics and morphology are available at https://github.com/aelefebv/Mitometer-Supplement. LSM image files collected through Zeiss' Zen software version 2.3 SP1 were converted to Tifs in ImageJ v1.53c. All FLIM data collected through SimFCS version 4 were referenced to the calibration sample in SimFCS version 4. Random forest classification was implemented via Scikit-learn's Python packages. All other statistical analyses were done through Graphpad Prism version 7.

For manuscripts utilizing custom algorithms or software that are central to the research but not yet described in published literature, software must be made available to editors and reviewers. We strongly encourage code deposition in a community repository (e.g. GitHub). See the Nature Research guidelines for submitting code & software for further information.

Data

Policy information about availability of data

All manuscripts must include a data availability statement. This statement should provide the following information, where applicable:

- Accession codes, unique identifiers, or web links for publicly available datasets
- A list of figures that have associated raw data
- A description of any restrictions on data availability

The authors declare that all data supporting the findings of this study are available within the article and its supplementary information files or from the corresponding author upon reasonable request.

Field-specific reporting

Please select the one below that is the best fit for your research. If you are not sure, read the appropriate sections before making your selection.

☒ Life sciences ☐ Behavioural & social sciences ☐ Ecological, evolutionary & environmental sciences

For a reference copy of the document with all sections, see nature.com/documents/nr-reporting-summary-flat.pdf

Life sciences study design

All studies must disclose on these points even when the disclosure is negative.

Sample size	No statistical tests for sample size determination were performed. Instead, as many cells as possible were imaged within one hour of treatment with the mitochondrial dye to ensure replicability. For the fission and fusion time lapse experiments, as many cells as possible were imaged before the next time point. Each experiment provided enough mitochondria for significant statistical tests. We also ensured that each group had mitochondria originating from at least 10 individual cells, a number exceeding typical numbers in the field. The total number of mitochondria analyzed for each condition was substantially greater than typical numbers used within the field.
Data exclusions	No data were excluded from analyses presented in the manuscript unless otherwise specified.
Replication	Mitochondria were analyzed within at least 10 individual cells for each experiment unless otherwise specified. All other simulation based replications are enumerated in the respective figures but were at least 3. All attempts at replication were successful.
Randomization	No randomization was performed. Specific cells chosen for imaging and subsequent analysis were not chosen by any specific metric. Samples were allocated into groups based on breast cancer subtype, or lack thereof. Randomization in these experiments were not technically feasible, and its impact was considered negligible. Thus the substantial effort that would have been required to implement it was not justified.
Blinding	The analysis for experiments comparing different conditions is inherently blinded as the softwares take no subjective user input.

Reporting for specific materials, systems and methods

We require information from authors about some types of materials, experimental systems and methods used in many studies. Here, indicate whether each material, system or method listed is relevant to your study. If you are not sure if a list item applies to your research, read the appropriate section before selecting a response.

Materials & experimental systems

n/a	Involved in the study
☒	☐ Antibodies
☐	☒ Eukaryotic cell lines
☒	☐ Palaeontology and archaeology
☐	☒ Animals and other organisms
☐	☒ Human research participants
☒	☐ Clinical data
☒	☐ Dual use research of concern

Methods

n/a	Involved in the study
☒	☐ ChIP-seq
☒	☐ Flow cytometry
☒	☐ MRI-based neuroimaging

Eukaryotic cell lines

Policy information about cell lines

Cell line source(s)	MCF10A, MCF-7, T-47D, MDA-MB-231, MDA-MB-468, BT-549, PC12, H1299, HFF, MEF, and HeLa cells were obtained from the American Type Culture Collection (ATCC).
Authentication	The cell lines were not authenticated.
Mycoplasma contamination	The cell lines were not confirmed to be mycoplasma-free.
Commonly misidentified lines (See ICLAC register)	No commonly misidentified cell lines were used.

Animals and other organisms

Policy information about studies involving animals; ARRIVE guidelines recommended for reporting animal research

Laboratory animals	HCI-010 and HCI-002 PDX tumors were established and grown in 3-4-week old female NSG mice purchased from The Jackson

Laboratory animals	Laboratory (Bar Harbor, Maine, USA). Animals were maintained in a pathogen-free facility with a controlled 12/12–h light/dark cycle (lights on at 6:00 AM), temperature (22 ± 2°C), and relative humidity (45%–65%).
Wild animals	The study did not include the use of wild animals.
Field-collected samples	The study did not include field-collected samples.
Ethics oversight	Animal procedures were approved by the University of California, Irvine, Institutional Animal Care and Use Committee.

Note that full information on the approval of the study protocol must also be provided in the manuscript.

Human research participants

Policy information about studies involving human research participants

Population characteristics	Samples from patients were generously provided by A.L. Welm in the Department of Oncological Sciences at the Huntsman Cancer Institute (HCI). Briefly, HCI002 was acquired from a primary tumor biopsy of a female patient diagnosed with ER-PR-Her2-, basal-like Stage IIIA medullary type IDC with no previous systemic treatment. HCI010 was acquired from a pleural effusion of a Stage IIIC female patient diagnosed with ER-PR-Her2-, basal-like (PAM50) IDC treated with several rounds of chemotherapies. Human breast reduction mammoplasty samples were obtained through the Cooperative Human Tissue Network (CHTN). All covariate-relevant population characteristics of the human research population (e.g. age, gender, race) is available in the supplementary materials.
Recruitment	All tissue samples were collected with informed consent from individuals being treated at the Huntsman Cancer Hospital and the University of Utah. No self-selection bias or other biases were present in conducting these studies that the authors are aware of.
Ethics oversight	Samples were collected and de-identified by the Huntsman Cancer Institute Tissue Resource and Application Core facility before being obtained for implantation under a protocol approved by the University of Utah Institutional Review Board. We were able to obtain human reduction mammoplasty samples under the approved IRB protocol UCI 17-05.

Note that full information on the approval of the study protocol must also be provided in the manuscript.